



Review

Recent advances in computational methods for measurement of dendritic spines imaged by light microscopy

Shigeo Okabe *

Department of Cellular Neurobiology, Graduate School of Medicine, The University of Tokyo, Tokyo 113-0033, Japan

*To whom correspondence should be addressed. E-mail: okabe@m.u-tokyo.ac.jp

Received 16 August 2019; Editorial Decision 23 March 2020; Accepted 23 March 2020

Abstract

Dendritic spines are small protrusions that receive most of the excitatory inputs to the pyramidal neurons in the neocortex and the hippocampus. Excitatory neural circuits in the neocortex and hippocampus are important for experience-dependent changes in brain functions, including postnatal sensory refinement and memory formation. Several lines of evidence indicate that synaptic efficacy is correlated with spine size and structure. Hence, precise and accurate measurement of spine morphology is important for evaluation of neural circuit function and plasticity. Recent advances in light microscopy and image analysis techniques have opened the way toward a full description of spine nanostructure. In addition, large datasets of spine nanostructure can be effectively analyzed using machine learning techniques and other mathematical approaches, and recent advances in super-resolution imaging allow researchers to analyze spine structure at an unprecedented level of precision. This review summarizes computational methods that can effectively identify, segment and quantitate dendritic spines in either 2D or 3D imaging. Nanoscale analysis of spine structure and dynamics, combined with new mathematical approaches, will facilitate our understanding of spine functions in physiological and pathological conditions.

Key words: dendritic spine, computational analysis, super-resolution microscopy, structured illumination microscopy, synapse, machine learning

Introduction

Dendritic spines, small protrusions formed on the surface of dendritic shafts [1], contact presynaptic axons to form excitatory synaptic junctions. Presynaptic and postsynaptic membranes interact mechanically via cell adhesion molecules, which regulate accumulation of postsynaptic glutamate receptors and stabilize the synaptic junction [2,3]. Spine morphology varies widely [4]: some spines are large and mushroom-shaped [5]; others are thin and lack enlarged heads; and still others are ‘stubby’, i.e. short and thick without detectable necks [6]. Clear borders between mushroom, thin and stubby spines are difficult to define, and the variation in spine shapes may be more accurately conceived as a continuum [7].

Spine morphology is linked to the properties of the intra-spine cytoplasm. The main cytoskeletal component within spines is filamentous (F)-actin [8]. F-actin is the major determinant of the spine shape, as demonstrated by the observation that the actin-depolymerizing reagent latrunculin induces rapid shrinkage of spine heads. The spine cytoplasm also contains membrane-bound organelles, including the smooth endoplasmic reticulum (sER), spine apparatus and endosomal vesicles [9–11]. Spines containing membrane organelles are generally larger, whereas thin spines are less likely to contain organelles. Thus, spine morphology is correlated with the content of membrane-bound organelles. Sub-membranous structures are also important in spine function. In particular,

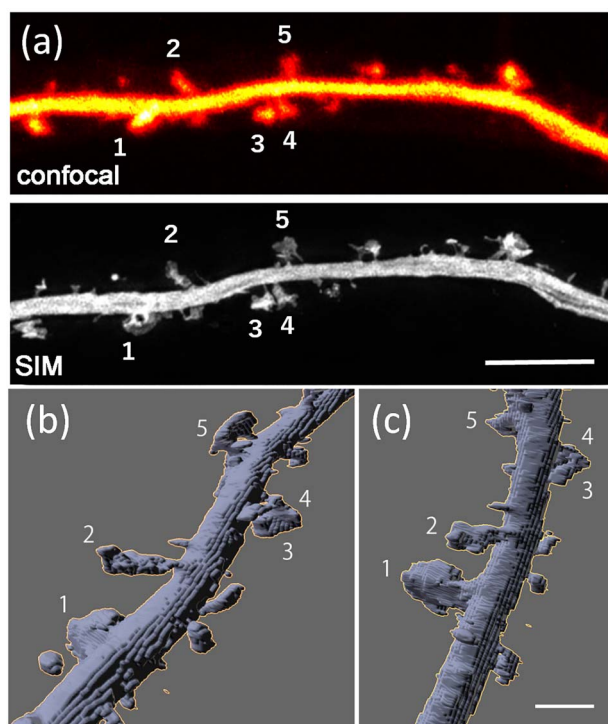


Fig. 1. A dendrite of a cultured hippocampal neuron, imaged by confocal microscopy or SIM. (a) Confocal and SIM imaging of a hippocampal neuron dendrite expressing GFP. Numbers indicate locations of five spines. Spine 1 is difficult to identify in this confocal image. Bar, 4 μm. (b) Spines and shaft reconstructed from SIM images, taken from the same dendritic segment shown in (a). Numbers correspond to the five spines shown in (a). The dendrite is viewed obliquely from the xy-plane. (c). The same spines and shaft, reconstructed from SIM images, viewed perpendicular to the optical axis. Spine 1, which is difficult to detect in (a), protrudes above the shaft. Bar, 1 μm.

the postsynaptic density (PSD), which is located at synaptic junctions, is composed of a multitude of membrane molecules and postsynaptic scaffolding molecules [12]. Membrane molecules in the PSD include glutamate receptors, cell adhesion molecules and receptors for growth factors and cytokines. PSD scaffolding molecules contain multiple binding domains, arranged in tandem, that can bind to glutamate receptors and cell adhesion molecules. PSDs are disk-like structures with diameters of about 500 nm [13]. Both PSD size and the functional glutamate receptor content of a synapse are correlated with spine size. Together, these data indicate that spine size is correlated with synaptic efficacy and that this relationship is based on the role of PSDs in accumulating glutamate receptors to synaptic junctional sites [14].

Spines are not stable structures but instead change their shapes over time [15]. These structural changes can be divided into two conceptual categories, the first of which is activity dependent [1]. Spine expansion can be induced by presynaptic stimulation as well as by uncaging of glutamate near the spine head [16]. This spine expansion can be inhibited by NMDA receptor blockade, removal of extracellular calcium or F-actin depolymerization, indicating that active actin remodeling by NMDA receptor-dependent calcium influx underlies activity-dependent spine expansion. Synaptic efficacy is determined by both presynaptic parameters and postsynaptic sensitivity to neurotransmitters. In the excitatory synapses, the postsynaptic

content of AMPA-type glutamate receptors is the most important factor that regulates changes in synaptic efficacy in the process of long-term potentiation (LTP). Activity-dependent spine expansion is associated with an increase in the surface AMPA receptor numbers and is thought to be an important structural component in LTP [1,6]. The second category is spontaneous fluctuation of spine structure [17,18]. Spines contain a high density of F-actin, and actin-rich structures (e.g. filopodia and lamellipodia in fibroblasts) tend to undergo rapid structural remodeling [19]. Imaging studies have shown that spines undergo morphological remodeling on the multiple time scales from minutes to months [20,21]. Both activity-dependent expansion and spontaneous fluctuation of spine structure are thought to be important in the transition from nascent to mature spines and increase of their stability in postnatal development.

Both light and electron microscopy (EM) techniques are useful for recording the structures of dendritic spines as well as their temporal changes in response to neural network activity. Methods for reconstructing spine morphology by EM have a history spanning more than three decades; over that time, the development of useful algorithms and computer programs has helped researchers to efficiently obtain quantitative data. By contrast, methods for detecting, segmenting and quantitating dendritic spines from light microscopic images are more challenging and remain under development. In this review, we will summarize the current state of spine detection and measurement based on light microscopic data. We close by discussing future directions for this field, which will require further progress in microscopy and computational science.

Imaging of dendritic spines by light microscopy

Spine shape analysis requires high-resolution images, and the choice of light microscopic modality is an important determinant of the precision and accuracy of these measurements. The choice of imaging modality also depends on the types of biological samples. Application of conventional wide-field fluorescence microscopy in spine imaging is limited to thin samples, such as a dissociated culture of neurons, as this method is not effective in blocking fluorescence signals derived from fluorescent objects outside of the focal plane. A combination of wide-field microscopy with light sheet illumination is one possible solution for application to thicker samples. Samples of neurons in a tissue environment can be prepared by cutting brain sections with or without prior fixation or by making organotypic slice cultures. The thickness of these samples ranges from 50 to 300 μm, which requires optical sectioning by scanning microscopy, including techniques such as confocal laser scanning microscopy (CLMS) and two-photon excitation laser scanning microscopy (2PLSM). Finally, the structure and function of neurons integrated into the neural network of the intact brain can be detected by *in vivo* 2PLSM.

In addition to these conventional optical methods, which are limited by light diffraction, new technologies for super-resolution imaging have begun to be applied to spine imaging [19,22,23]. Super-resolution techniques based on wide-field microscopy [structured illumination microscopy (SIM) and single-molecule localization microscopy, which includes photoactivated localization microscopy (PALM) and stochastic optical reconstruction microscopy (STORM)] are better suited to thin samples, e.g. dissociated neurons in culture (Fig. 1). Recent efforts of combining these technologies with more restricted sample illumination methods, such as light sheet illumination, will enable the application to thick samples. On the other hand, scanning microscopy-based super-resolution imaging, such as

stimulated emission detection (STED) microscopy, can be applied to thicker samples [24] and even *in vivo* imaging [25]. Because the sizes of dendritic spines range from several hundred nanometers to a few micrometers, the diffraction limit of conventional light microscopy (200 nm in the horizontal plane and 400 nm in the vertical dimension, assuming ideal imaging conditions and an objective lens with a high numerical aperture) severely limits the accuracy of spine shape measurements. Comparison of spine images obtained by STED and two-photon microscopy, together with spatial filtering of the STED images to mimic two-photon resolution, reported the risk that short-necked spines may be wrongly classified as stubby spines due to lower optical resolution of two-photon microscopy [7]. Super-resolution imaging has clear advantages for quantitative analysis of spine shape and dynamics. A possible disadvantage of super-resolution imaging is a relatively high dose of excitation light and its adverse effects in live imaging. Recent progress in the optimization of imaging conditions is beneficial for long-term observation of light-sensitive cells [26].

In tissue environments, dendritic shafts run in multiple directions, and attached spines protrude without an orientation preference relative to the longitudinal axis of the shaft. Because the vertical resolution of light microscopy is lower than its horizontal resolution, the accuracy of spine images depends on orientation: spines that protrude within the *xy*-plane can be imaged with higher accuracy than those that protrude along the *z*-axis. In addition, vertically protruding spines are positioned above or below dendritic shafts and may become difficult to separate from their parent shafts if their lengths are close to the *z*-axis optical resolution. Imaging conditions and spine analysis that facilitate detection of vertically protruding spines may be necessary for unbiased measurement of spine density.

For reliable detection of spines, fluorescent probes must be optimized. The most widely used fluorescent probes for spine imaging are green fluorescent protein (GFP) and related fluorescent proteins. To increase the fidelity of spine detection, co-expression of another fluorescent probe that localizes to PSD would be useful. Expression of GFP- and red fluorescent protein (RFP)-tagged version of the major PSD scaffolding molecules PSD-95 and Homer is useful for spine synapse detection both *in vitro* [27,28] and *in vivo* [29–31]. Although GFP and other fluorescent proteins are reliable probes, they cannot be used to detect neuronal morphology in human samples. For this purpose, detection of dendritic spines in postmortem tissue can be achieved by intracellular injection of lucifer yellow [32]. Because the surface-to-volume ratio of dendritic spines is higher than that of dendritic shafts, probes that associate with the plasma membrane are useful for boosting fluorescence signals emitted from spines.

Strategies for automated detection of dendritic spines

Traditionally, dendritic spines are detected manually and measured by human operators. These manual strategies require considerable time and effort, precluding their routine application to the analysis of large amounts of imaging data. To address this issue, several principles for automated spine detection have been proposed over the past decade. Spine detection protocols can be grouped into two categories: those that analyze 2D projection images based on their geometry in the *xy*-plane and those that analyze three-dimensional (3D) images based on their volume and surface characteristics.

Spine detection in 2D dendritic images

Spine detection methods that use 2D images apply automated image processing to either a single projection image generated from an original 3D image stack or a single image plane containing target spine structures from *z*-stack images. These approaches are useful for spine detection from image data obtained by wide-field fluorescence microscopy, CLSM, 2PLSM and also several super-resolution imaging techniques. In the case of wide-field fluorescence microscopy and CLSM, dendrites and spines horizontally oriented in dissociated neuronal cultures are suitable for analysis based on 2D images. For 2PLSM, analysis based on 2D images is suitable if the imaging conditions involve lower *z*-axis resolution and wider *z*-axis sectioning. In such a case, spines above and below dendritic shafts are less likely to be resolved, and spine detection is practically restricted to spines protruding in the horizontal direction.

The first strategy for spine detection in 2D images is based on generation of skeleton images of dendrites [33,34]. These skeletons are extracted by iterative deletion of successive layers of pixels on the image boundary (Fig. 2a). Using this technique, Bai *et al.* detected spines by searching for endpoints of protruding branches in the skeleton, shorter than 4 μm , in 2PLSM image stacks obtained from GFP-expressing hippocampal neurons in organotypic slices [35]. Spine detection based on skeletons requires appropriate binarization of the original images and extraction of all spines that remain attached to dendritic shafts. When some spines become detached during the process of binarization, they must be re-merged through additional processing. Cheng *et al.* followed a similar strategy: they generated skeleton images from 3D 2PLSM image stacks and then detected spines as short branches from the main line of the skeleton [36]. They identified detached spines by evaluating the local signal-to-noise ratio (SNR) and setting a threshold for the SNR above which local pixel clusters were classified as spines. A similar method for skeleton image generation was applied to the analysis of spine morphological changes in wide-field time-lapse fluorescence images of dissociated hippocampal neurons in culture [37]. Moreover, the method of skeletonization can be combined with other protocols for spine detection. Rada *et al.* proposed a spine detection method based on generation of a skeleton image, endpoint detection using this skeleton and further confirmation of the endpoints as spines by application of dot enhancement filters [38,39]. Dot enhancement filters, which are based on eigenvalue analysis of the Hessian matrix (a square matrix of second-order partial derivatives), can be used to isolate structures based on their similarity to nodule-like objects [40]. Dot enhancement filters with appropriate scale ranges are useful for isolation of spine-like structures and can be combined with alternative methods of endpoint detection.

The second strategy involves identification of spines by first defining the boundary of the dendritic shaft and then isolating spines as objects outside of the boundary (Fig. 2b). Su *et al.* proposed a protocol based on this idea [41]. Using iterative image processing methods, including directional morphological filtering [42], small round structures near the dendritic shaft can be effectively removed. After this iterative process, the boundary of the dendritic shaft is identified by calculating the intensity gradient values of the extracted dendritic shaft and finding the shortest path along the pixels of high-intensity gradient values. Image pixels belonging to spines are defined as pixels outside the boundary of the dendritic shaft.

Wang *et al.* reported a method for defining the boundary of dendritic shafts using conditional symmetric analysis [43]. They proposed that the wavelet transform of dendritic images is useful in identification of pairs of dendritic contours and determination of

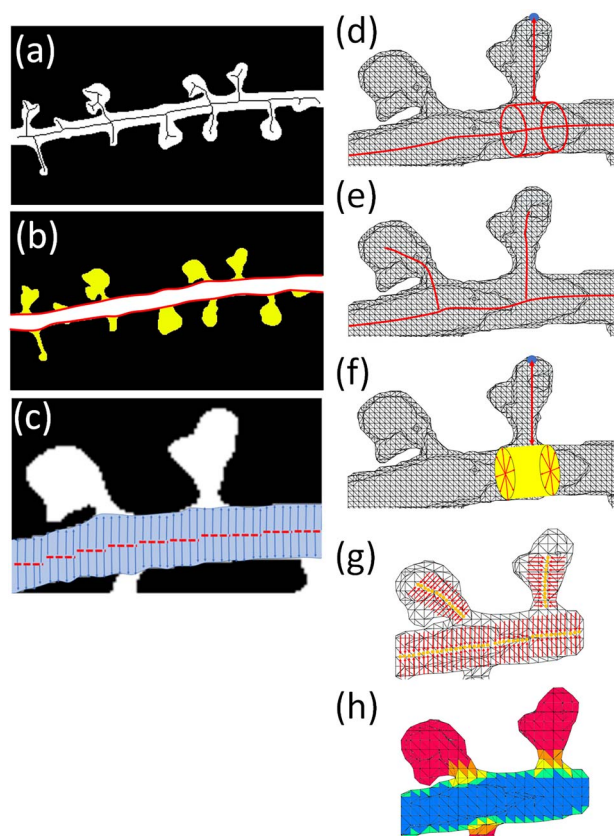


Fig. 2. Methods for spine detection in either 2D or 3D imaging data. (a) Spine detection in 2D images based on generation of skeleton images. Iterative deletion is performed on successive layers of pixels on the image boundary, leaving the skeleton at the center of the image object. (b) Spine detection in 2D images by defining the boundaries of dendritic shafts (red lines). The areas outside the boundary are identified as spines (yellow areas). (c) Spine detection in 2D images using a curvilinear structure detector. The centerline of the shaft (red dotted line) is determined from the local line directions (arrows) of the intensity gradient. (d) Spine detection in 3D images based on generation of skeleton images. From the position of the centerline, the surface position of the shaft is estimated (red circles). Spine tips are detected as voxels with the largest local distance from the backbone that are also outside the shaft surface. (e) Spine detection in 3D images based on generation of skeleton images. The curve skeleton is analyzed to detect branch points and short branches corresponding to spines. (f) Spine detection in 3D images based on estimation of shaft surfaces by Rayburst sampling. Multidirectional rays from the local points are used to detect the shaft surface (red arrows). Spine tips are detected as voxels with the largest local distance from the shaft surface. (g) Spine detection in 3D images based on gradient vector flow. Gradient filters generate vectors that point to the central regions of local objects (red arrows). The central regions of spines are determined based on these vectors (yellow circles). (h) Spine detection in 3D images based on surface features. Specific values reflecting geometric features are mapped to the vertices of the surface mesh. Red regions correspond to the vertices with larger distances to the shaft backbone and higher mean curvature.

the centerline of the shaft. In their technique, the boundary of the dendritic shaft is set by identifying the points where pixel intensity decreases sharply along the line perpendicular to the centerline, and the boundary of the dendritic shaft is used to define the junction between the shaft and the spines.

The third approach is the application of a curvilinear structure detector [44] for extraction of the centerlines and boundaries of the dendritic shafts and spines (Fig. 2c) [45–47]. During this process,

a Hessian matrix is generated for each image pixel, and the direction of the eigenvector corresponding to the maximum absolute eigenvalue for each pixel is mapped. This direction is perpendicular to that of linear objects or linear patterns of intensity changes. Using local line directions, the centerline of the object can be determined. This centerline detection protocol can be applied to detect centerlines of both dendritic shafts and spines. In addition, the boundary between fluorescent objects and background can be detected as points where the second-order derivative changes abruptly.

Spine detection in 3D dendritic images

Spine detection methods for 3D images are designed to handle voxel data and effectively identify dendritic spines that protrude not only in the horizontal plane but also vertically above and below the dendritic shafts. As two-photon microscopy has been more widely adopted for imaging of the complex 3D structures of dendrites in thick slice preparations and *in vivo*, the need for efficient protocols for spine detection in 3D images has increased.

The first strategy for spine detection from 3D images is based on generation of skeleton images of dendrites by iterative deletion of successive layers of pixels on the image boundary, as described above for 2D image processing [48]. Once the centerlines of dendrites have been determined, the tips of protrusions on the dendrite surface are identified as the voxels with the largest local distances from the backbone voxels of the shaft (Fig. 2d). Spine candidates are separated from the shaft using the shaft surface, which is estimated by locally fitting the shaft with a cylinder. Skeletonization of dendrites and spines can also be achieved from surface representations of these objects [49]. After detection of dendrite and spine surfaces, a curve skeleton is detected using a medial geodesic function [50]. The curve skeleton is analyzed to identify branches, and spines are detected based on their lengths and local radii (Fig. 2e). Singh *et al.* [51] used the centerline detection approach with an image preprocessing algorithm that enhances voxels belonging to spines and applied the combined technique to automated 3D spine detection from *in vivo* two-photon image stacks.

The second strategy for 3D spine detection is the protocol proposed by Rodriguez *et al.* [52–54], which is implemented in the widely used program NeuronStudio. They used Rayburst sampling to measure local dendrite diameters (Fig. 2f). Rayburst sampling casts a multidirectional core of rays from an interior point of a cylindrical object onto its surface; the rays' shortest length can be used as the local diameter. Precise 3D fitting of even highly varicose dendrites can be achieved by repeating Rayburst sampling along the longitudinal direction of the dendrite. After detection of the dendritic shaft using this procedure, Rodriguez *et al.* calculated the distance to the surface of the dendritic shaft for each voxel outside of the shaft voxels. The local maxima of these values, calculated from 26 connected candidate neighbors (corresponding to a cubic composed of $3 \times 3 \times 3$ voxels), were taken as candidate spine tips. For each spine tip candidate, voxels grouped as a single spine were identified by iterative expansion of voxels from the tip toward the dendritic shaft. This expansion process helps to avoid double counting of single spines with two local maxima that are detected as spine tip candidates. A similar approach for detecting the centerline and radii of dendritic shafts using ray sampling was reported by Shi *et al.* [55].

The third approach for 3D spine detection is the application of gradient vector flow to detect central regions of dendrites and spines (Fig. 2g). Zhang *et al.* designed a gradient filter that points to the central regions of local objects and utilized this technique to

detect regions that correspond to either the centerline of dendrites or those of spines [56]. After detection of the central regions of either shafts or spines, they classified the objects containing these central regions based on their shape characteristics. This was achieved by calculation of the Hessian matrix and its eigenvalues, which represent specific shapes such as blobs, tubes and plates, similar to the principle described above for dot enhancement filters. Spines can be classified as small objects with shapes that have features of both tubes and blobs.

Spine detection can also be achieved by analysis of 3D surface features. Qing Li *et al.* [57] proposed a method for spine detection using three geometric features: distance to the dendrite backbone, mean curvature of the surface and normal variance of the surface (Fig. 2h). To calculate the distance to the dendrite backbone, they used Rayburst sampling, as in the technique of Rodriguez *et al.* [53]. The local surfaces of spines should have larger values for all three geometric features. Accordingly, for spine detection, a score map of the dendrite surface with the summed value of three geometrical features is generated. The tips of spines can also be detected as the local surface where the minimal cross-sectional curvature takes the maximal value. Using this property, He *et al.* [58] proposed a protocol for spine detection based purely on the surface characteristics of spines.

A multi-scale opening algorithm can separate two conjoined fuzzy objects with different intensity properties but an overlapping shared intensity band [59]. Basu *et al.* applied this algorithm for detection and separation of dendritic spines from dendritic shafts [60]. In their method, after segmentation of the image stack, spines are isolated from dendrites by gradual erosion of the assembly of two fused objects (spine and dendrite) until the two objects become mutually disconnected. Because the image intensities of spine voxels are lower than those of shaft voxels, this intensity difference can be used to calculate membership functions that determine whether a voxel in the shared intensity band should be classified as a spine or dendrite voxel.

If ground-truth data are available for spine distribution, a model-based approach for spine classification becomes feasible. Blumer *et al.* [61] performed two-photon imaging of live pyramidal cell dendrites and followed up with ultrastructural analysis of the same dendrites by serial block-face scanning EM (SBEM). In their approach, based on the SBEM data, synthetic fluorescence images are generated by point spread function (PSF) convolution. The training data for the statistical model of spine probability consists of the synthetic fluorescence images combined with the SBEM data (representing the ground truth). This statistical model is based on the cross-sectional images of dendrites orthogonal to the dendrite backbone. If spines are sectioned, these cross-sectional images should have intensity distributions along the orientations of protruding spines. Based on this idea, spine probability models for eight orientation-dependent spine intensities (radial 45° segments) are generated and compared with the synthetic fluorescence images using principal component analysis (PCA).

Finally, 3D spine analyses have been proposed based on commercially available imaging software. Swanger *et al.* [62] reported that it is possible to achieve accurate 3D tracing of dendrites using neurons expressing Lifeact-Ruby in combination with Filament Tracer (Imaris, Bitplane), a commercially available 3D tracing program. For appropriate spine detection, several parameters must be manually specified, including the minimum spine end diameter and the maximum spine length. In another example of this approach, Toharia *et al.* [63] used Filament Tracer to detect dendritic spines in human pyramidal neurons intracellularly injected with lucifer yellow.

Strategies for automated segmentation of dendritic spines

After detection of dendritic spines, the boundary between spines and dendritic shafts must be determined. Spine morphology varies widely, and there is no clear morphological landmark at the junction between spines and dendritic shafts. Researchers have proposed a variety of mathematical principles and protocols for the segmentation of spines for more objective and unbiased segmentation. Here again, the methods can be grouped into two categories: those based on 2D projection images and those based on 3D information derived from image stacks.

Spine segmentation in 2D dendritic images

Segmentation of spines is straightforward if the boundary of the dendritic shaft has already been detected for the purpose of isolating spines as objects outside of this boundary. As already stated in the section on spine detection, Su *et al.* [41] and Wang *et al.* [43] followed this approach and defined the boundaries of dendrites before the step of spine detection.

When the protocol for spine detection is based on generation of skeleton images of dendrites, additional steps are required to determine the boundary between dendritic shafts and spines. To this end, one simple strategy is to set the segmentation positions at the bases of spines (Fig. 3a). Bai *et al.* [35] adopted this strategy of defining the line that passes the segmentation position and runs parallel to the local direction of the dendrite's centerline. The segmentation positions are specified by following several rules that aid in detection of spine bases. Cheng *et al.* [36] adopted the strategy of dendrite backbone extraction for spine detection. They estimated the local thickness of the dendrites using a calculation designed to exclude spine boundary pixels. Pixels in the local region that have a distance larger than the local thickness are taken as spine pixels. A similar approach for spine pixel detection was used by Fan *et al.* [45].

The second type of spine segmentation strategy is based on the detection of local intensity features of spines (Fig. 3b). After detection of the backbone of the dendritic shaft, Choy *et al.* [46] detected local intensity peaks with defined distances from the backbone. Subsequently, they used a seeded watershed algorithm to segment spines. To achieve proper segmentation, spines detected by dot enhancement filters also require additional local intensity-based calculations. Son *et al.* [37] utilized the thresholding technique of geodesic active contours to achieve spine segmentation after spine heads were detected using dot enhancement filters. Geodesic active contours are based on deforming an initial contour toward the boundary of the object and can tolerate large variations in intensity gradients. The combination of watershed segmentation and the geodesic active contour algorithm has also been successfully applied to spine segmentation following detection using dot enhancement filters [38,39].

As mentioned above, a curvilinear structure detector is useful for extraction of the centerlines and boundaries of dendritic shafts and spines [45,47]. Therefore, this method can be directly used to detect boundaries between spines and dendrites (Fig. 3c). The edges of spines and dendritic shafts detected by a curvilinear structure detector overlap at spine-shaft boundaries.

In summary, spine segmentation approaches in 2D images depend on the preceding procedures of spine detection. The three major approaches are segmentation based on detection of the dendritic shaft boundary, segmentation based on local intensity features and segmentation using a curvilinear structure detector.

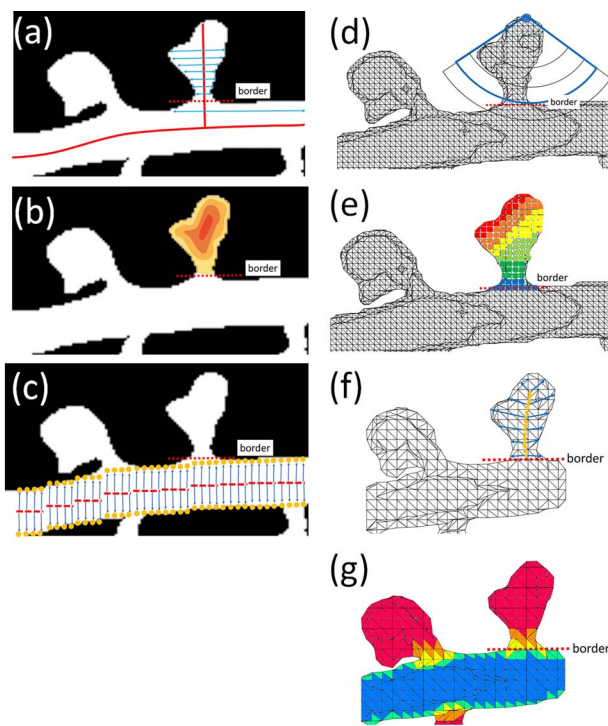


Fig. 3. Methods for spine segmentation using either 2D or 3D imaging data. (a) Spine segmentation in 2D images after generation of skeleton images of dendrites. From the spine tip, a line perpendicular to the shaft centerline is generated. The width of the spine is measured along this line (blue arrows), and the position from the narrow neck to the wide spine base is determined (red dotted line). (b) Spine segmentation in 2D images based on detection of local intensity features. The local intensity peak within the detected spine area is identified (red area), and a seeded watershed algorithm is used to identify the border (red dotted line). (c) Spine segmentation in 2D images based on the application of a curvilinear structure detector. In this method, boundaries between spines and shafts can be estimated from an analysis of the intensity gradient (yellow circles). (d) Spine segmentation in 3D images after generation of skeleton images. From the spine tip, spheres with increasing diameters are generated, and the optimal sphere that contains all spine voxels but excludes voxels of the shaft is selected (blue curve and line). (e) Spine segmentation in 3D images using iterative addition of new voxel layers starting from the spine tip (red voxels). When the voxel layer reaches the spine base, iteration is terminated (blue voxels). (f) Spine segmentation in 3D images following spine detection by gradient vector flow. In this protocol, the central regions of the spines were detected previously (yellow circles). From these seed points in the central region, the fast marching algorithm was applied (blue arrows) to detect all voxels belonging to the spine. (g) Spine segmentation in 3D images based on spine surface characteristics. In this case, local geometric features were previously mapped to the surface, and appropriate thresholding of the surface effectively determined the border.

Spine segmentation in 3D dendritic images

In many programs for analyzing spines using 3D images, spines are detected based on the voxels of their tips, which are locally furthest from the shaft backbone or shaft surface. Therefore, the spine segmentation protocols in these programs use iterative methods to determine the spine–shaft boundaries, using the identified spine tips as seed voxels. Using this strategy, Koh *et al.* [48] generated a series of candidate spines of different sizes by grouping voxels within spheres of differing radii with a common center at the spine tip (Fig. 3d). The best candidate spine was selected based on the criterion that the base of the candidate voxel group had to terminate at the surface of the dendritic shaft. Singh *et al.* [51] used a similar strategy to

segment spines by determining the appropriate radius of a sphere with its center at the spine tip voxel and its radius equal to the distance between the spine tip and the shaft surface. Rodriguez *et al.* [52] also calculated the distance to the surface of the dendritic shaft for each voxel outside the shaft and then selected the local maxima calculated from 26 connected candidate neighbors as candidate spine tips (Fig. 3e). Subsequently, new voxel layers were iteratively added to the voxel of the spine tip candidate. All 26 connected neighbors of the previous layer were added. In this iterative process, if a newly added layer of voxels exceeded a predefined maximum spatial spread from the spine base, cluster building was terminated. Shi *et al.* [64] also detected the voxels of spine tips first but took a different approach to generating a series of cross-section images of the spines. In their method, a line is defined perpendicular to the dendrite backbone and passing the spine tip, and then multiple spine cross-sections are generated at uniform intervals along that line. Using wavelet transformation, the segmentation position along the perpendicular line can be defined by the sudden change in the wavelet response.

The gradient vector flow-based method can detect the central regions of dendritic protrusions and is therefore useful for spine detection (Fig. 3f). In this case, spine segmentation can be achieved using the fast marching algorithm [56]. In this algorithm, seed points are set at voxels within the spine's central region, and then a forward-moving boundary is calculated that moves with a speed function specified by the gradient vectors. After sufficient iteration of the forward movement of the boundary, all of the voxels of a given spine are covered, and segmentation is complete.

A unique approach is spine detection and segmentation by multi-scale opening algorithm, as proposed by Basu *et al.* [60]. Their technique integrates the process of spine identification and spine segmentation by separating two conjoined fuzzy objects (a spine and a parental dendritic shaft) by gradual erosion.

Several spine detection protocols are based on the characteristics of spine surface geometry. In these algorithms, surface mapping of local geometric features that match the characteristics of the spine can be used to segment the surface (Fig. 3g). For example, seed faces with their scores higher than the predetermined threshold are randomly selected, and the neighbor faces of the seeds are examined if they are also judged to have high scores. This process is repeated until all of the candidate spine surface areas are detected [57]. Spine tip detection by minimal cross-sectional curvature, described above, is also based on surface characteristics [58]. In this case, the values of the minimal cross-sectional curvature are mapped to the dendritic surface. From the face of the spine tip, iterative addition of neighbor faces with high values of minimal cross-sectional curvature is performed until the values fall below a predetermined threshold.

Segmentation of spines in 3D dendrite images requires more complex computation to assess spine–shaft borders. In general, iterative spreading strategies of spine voxels or faces belonging to spine surfaces are feasible for segmentation of the complex 3D shapes of spines.

Measurement of spine shape and classification

Spine morphology is highly variable, and multiple principles for spine classification have been proposed [6]. One widely applied approach involves assigning spines to three major categories: thin, mushroom and stubby; an additional category, filopodia, refers to non-spine dendritic protrusions [5]. This conceptualization is useful for manually classifying spines and evaluating the differences in the

morphological features of spine populations. On the other hand, some researchers argue that spine morphology is a continuum rather than a set of discrete groups [7,14,17]. To resolve this controversy, we first need to define geometrical parameters that can be used for objective extraction of spine shape characteristics.

The conventional geometrical parameters of spines are length, width and volume. Measurements of spine volume are the least prone to artifacts, mainly because the total fluorescence intensity of a spine is reasonably well correlated with its volume. On the other hand, measurements of lengths and widths are more problematic due to the resolution limit of conventional light microscopy. Imaging of spines in 2D dendrite images has additional problems associated with artifacts derived from projection of oblique or perpendicular spines onto 2D planes, together with the possible escape of spines above or below dendritic shafts (Fig. 1). Accordingly, 2D spine measurements should be restricted to experiments that compare different experimental conditions under identical imaging conditions.

Spine shape measurement in 2D dendritic images

Spine shape measurements based on 2D projection images of dendrites have been extensively applied to the analysis of spine phenotypes in cultured neurons manipulated to overexpress or suppress specific genes. Due in large part to the development of automated light microscopic imaging systems that can analyze a large number of culture preparations exposed to different chemical compounds, this approach has become more important in the field of drug discovery. As noted above, the traditional morphological parameters of dendritic spines are length, width and volume (estimated from total fluorescence intensity). Several recent papers proposed new approaches for more detailed analyses of spine morphologies in 2D projection images. In the previous section, we introduced the usefulness of curvilinear structure detectors for both spine detection and segmentation. After segmentation based on a curvilinear structure detector, Zhang *et al.* [47] used Zernike moments, orthogonal moments defined by Zernike polynomials, to extract spine features. Spine images can be expressed as integration of Zernike moments through multiple orders. In the study by Zhang *et al.*, 36 Zernike moments were calculated and used as spine shape features. Zernike moment-based shape description is more general and less biased than selection of a few geometric features.

Another approach to the general description of 2D spine shapes was proposed by Ghani *et al.* [65,66]; their approach is based on the Disjunctive Normal Shape Models (DNSMs), which are parametric implicit shape models. A DNSM approximates the characteristic function of a shape as a union of convex polytopes, which are themselves represented as intersections of half-spaces in a 2D image. This type of representation of a Boolean function is known as the disjunctive normal form. When the number of convex polytopes is N and the number of half-spaces is M , the 2D spine shape is expressed by the parameter $[N \times M \times 3]$.

Automated spine detection can be combined with advanced computational analyses, especially automated classification and clustering analysis based on principles of artificial intelligence (AI). In a recent study, spines were classified using DNSM-based parameter extraction in combination with kernel density estimation and likelihood ratio tests [65]. The goal of that study was to categorize spines into the three conventional categories (mushroom, thin and stubby) in concordance with the labels assigned by human experts. The principles for spine classification were relatively simple: first, likelihood values were obtained from the nonparametric density

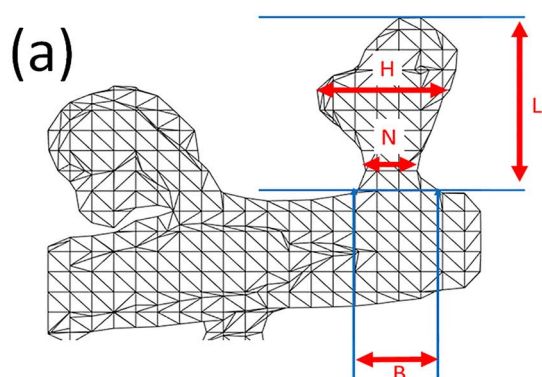
estimates of three spine classes, and then they were mapped to 2D decision regions. Notwithstanding its simplicity, the accuracy of this method was comparable to or better than those of other classification techniques, such as support vector machine (SVM) with a linear kernel or neural network-based classification using a two-layer back-propagation trained feed-forward network. Wang *et al.* [43] proposed regularized morphological shared-weight neural networks for classification of spines into the mushroom, thin and stubby types. Their system consisted of two-phase heterogeneous neural networks in series: the first phase extracted features via a hit-miss transform, and the second phase was a fully connected feed-forward neural network. The output of the second layer was a three-node layer in which each node corresponded to a spine type.

Spine shape measurement in 3D dendritic images

Descriptions of the 3D structure of spines require more morphological parameters than those based on 2D spine images. Because the resolution of imaging systems and voxel dimensions are not equal in the xy -plane or along the z -axis, the precision of measurement depends on direction, and this may introduce systemic errors in spine measurement. If morphological parameters are appropriately measured, information about 3D structure may help more accurately characterize and categorize a heterogeneous spine population.

The first approaches to 3D spine shape measurement involved setting a relatively small number of morphological parameters that could reasonably describe the overall shape characteristics. Janoos *et al.* [49] selected five parameters (length, volume, basal radius, maximum radius and minimum radius); the latter three parameters were measured in 2D maximum intensity projections. Other studies used more complex parameters for spine classification. Rodriguez *et al.* [52] classified spines using three parameters: aspect ratio (AR), head-to-neck ratio (HNR) and head diameter (HD) (Fig. 4a). In this method, AR reflects the ratio between the longitudinal and crosswise lengths of spines, and HNR is the ratio between the head and neck diameters. After these three parameters are calculated, spines are classified using the simple decision tree: If the neck is obvious (i.e. HNR is high) and the head is large (i.e. HD is high), the spine is classified as mushroom. If the neck is not clear (i.e. HNR is low) and the shape is thick (i.e. AR is low), the spine is classified as stubby. In other cases (high HNR and low HD or low HNR and high AR), the spine is classified as thin. Comparison of this automated spine classification with consensus data of manually classified spines revealed an 86% match, equal to or better than the best inter-human match rates. Basu *et al.* [60] took a similar approach to calculating a small number of key structural parameters: spine length (SL), neck length (NL), base-to-head distance (BH) and locally deepest point (CH) (Fig. 4b). The classification of spines was first based on the evaluation of NL: spines were classified as stubby when NL was zero. For spines with positive NL values, the positions of CH were analyzed; if CH positions were spread along the spine, it was classified as thin. By contrast, when CH positions were concentrated at the end of the spine, BH was evaluated; spines with high BH were classified as mushroom, and others were classified as spine-head protrusions. This approach could effectively detect structural differences among the four spine types.

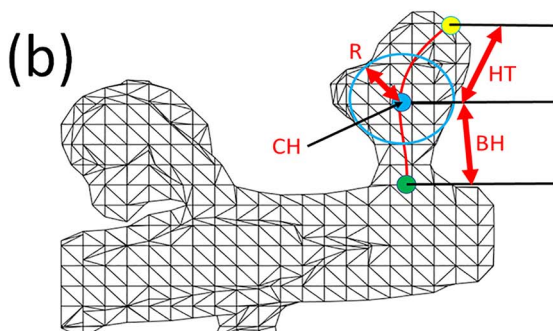
Other approaches to 3D measurement and classification are based on machine learning. Shi *et al.* [55,64] proposed a classification of spines by semi-supervised learning. To this end, they extracted seven morphological parameters of spines (HNR, head-to-length ratio, HD, neck diameter, maximum distance to dendrite surface, angle to



Aspect ratio (AR) = L / B
Head to neck ratio (HNR) = H / N
Head diameter (HD) = H

Spine classification Table

High HNR		High HD	Mushroom
High HNR		Low HD	Thin
Low HNR	High AR		Thin
Low HNR	Low AR		Stubby



Spine length (SL) = $HT + BH$
Neck length (NL) = $BH - R$

Spine classification Table

NL > 0		High BH/SL	Mushroom
NL > 0		Low BH/SL	Spine-head protrusion
NL > 0	CH spread along spine		Thin
NL = 0			Stubby

Fig. 4. Shape measurement in 3D spine images and spine classification. (a) Protocol proposed by Rodriguez *et al.* [52]. Three parameters (AR, HNR and HD) are calculated, and spines are classified into three categories based on their values. (b) Protocol proposed by Basu *et al.* [60]. Four parameters (SL, NL, CH and BH) are calculated, and spines are classified into four categories based on their values.

xy-plane, length) and also obtained a training dataset in which spines were labeled as mushroom, thin or stubby based on manual determination by human operators. To this dataset, the authors applied a method of semi-supervised learning [67] and classified spines into the mushroom, thin and stubby types. The error rate of classification was 20.1%, comparable to the performance of the classification method proposed by Rodriguez *et al.* (18.6%) [52].

Computational evaluation of 3D spine morphology may reveal new features of spines, leading to proposals for new spine classes. For example, Luengo-Sanchez *et al.* [68] generated surface mesh data

of dendritic spines and extracted 54 features that described their 3D morphology. Model-based clustering was applied to a dataset of 7916 individual spines, and six clusters were identified according to the Bayesian information criterion. Although the biological meaning of the six clusters has not yet been elucidated, these unbiased approaches to spine classification may be useful for identification of new functional subgroups of dendritic spines.

Application of automated spine detection, segmentation and measurement for specific experimental purposes

Multiple methods of automated spine detection, segmentation and measurement are described in the previous sections. For the selection of appropriate algorithms, programs and pipelines for spine analysis, it is helpful to provide comprehensive information about sample preparation, imaging conditions, morphological parameters, comparison with other methods and evaluation of performance. The information related to the literature discussed in this review is summarized in Tables 1 and 2. Each method is designed and optimized for the specific sample preparation and image acquisition conditions, and it is not appropriate to judge the performance of different methods with a single criterion. Practical guides for the selection of a suitable method can be summarized as follows:

First, the imaging conditions should be matched with the method of analysis. Some methods are designed for 3D image stacks with small voxel sizes (e.g. $0.05 \times 0.05 \times 0.11 \mu\text{m}$ [52]), which are suitable for high-resolution confocal imaging of *in vitro* preparations. Other methods are designed for 3D datasets obtained by two-photon microscopy, and voxel sizes are generally larger (e.g. $0.08 \times 0.08 \times 0.5 \mu\text{m}$ [51]). Datasets obtained from *in vivo* two-photon imaging specifically require reliable 3D tracing and fitting of dendritic shafts, which tend to run obliquely within the imaging volume [48].

Second, the availability and usability of the software should be considered. In some cases, the proposed algorithms are designed and implemented in specific computational environments and are not suitable for general applications. Some algorithms are based on more general platforms [39,69,70] or provided as standalone software [36,52,63], and it is not difficult to test their performance using real datasets.

Finally, spine shape differs between different cell types and may affect the performance of spine detection. For example, large mushroom spines can be reliably detected by either skeletonization or shaft boundary detection, but thin spines and small stubby spines are more difficult to identify by skeletonization. In the case of neurons with large mushroom spines, such as cerebellar Purkinje cells, skeletonization-based spine detection should be an appropriate approach. In turn, the skeletonization-based approach may give unreliable results when it is applied to immature cultured neurons, which contain filopodia and thin spines as predominant types of dendritic protrusions. In some reports, a direct comparison of the quantitative data obtained by light microscopy and electron microscopic reconstruction is presented and should be useful for the evaluation of the data reliability [61,70].

In summary, the selection of the best method for spine detection and analysis requires trials of multiple algorithms with real datasets. The conditions of image acquisition and sample properties can provide a general guide for the algorithm selection, but the performance of the algorithm applied to real datasets may not always

Table 1. List of sample types and image acquisition conditions

Ref. number	Sample type (culture, slice, <i>in vivo</i>)	Microscope (wide-field, confocal, two-photon)	Image acquisition condition
[33]	Lucifer yellow injected neurons in fixed brain slice of 200–400 μm	Confocal	Objective lens NA = 1.4, XY pixel size = $0.098 \times 0.098 \mu\text{m}$, 1024×1024 pixels in XY, 0.081 μm Z-spacing, 1000–1200 optical sections
[34]	Golgi staining and sections of 80 μm thickness	Wide-field	No information
[35]	Organotypic slice culture, biolistic transfection of GFP	Two-photon	Objective lens NA = 0.9, XY pixel size = $0.084 \times 0.084 \mu\text{m}$, 1.0 μm Z-spacing
[36]	Tissue section with GFP expressing neurons	Two-photon	Objective lens NA = 0.9, 1.0 μm Z-spacing
[37]	Rat hippocampal neurons in culture expressing GFP	Wide-field epifluorescence	Objective lens NA = 1.4, XY pixel size = $0.107 \times 0.107 \mu\text{m}$, 1112×941 pixels in XY, single plane time lapse every 5 s for 50 2D images
[38]	Not specified	Two-photon	14 different 2D images
[39]	Organotypic slice culture, biolistic transfection of Dendra-2 or AFP	Two-photon	Objective lens NA = 0.9, XY pixel size = $0.019 \times 0.019 \mu\text{m}$, 1024×1024 pixels in XY, 0.3 μm Z-spacing
[43]	Rat cortical neurons in culture, neurons transfected with GFP	Confocal	63 \times objective lens, XY pixel size = $0.24 \times 0.248 \mu\text{m}$, 1024×1024 pixels in XY, maximum intensity projection images were analyzed
[45]	<i>In vivo</i> cranial window preparation	Two-photon	XY pixel size = $0.06 \times 0.06 \mu\text{m}$, 512×512 pixels in XY, 0.5 μm Z-spacing, 15–20 images per Z-stack
[46]	DiI-labeled neurons	Confocal	40 \times objective lens NA = 1.3, 0.8 μm Z-spacing, maximum intensity projection images were analyzed
[47]	Pyramidal neurons transfected with GFP	Two-photon	42 \times 42 μm of image field, 1.0 μm Z-spacing
[48]	Organotypic slice culture	Two-photon	40 \times objective lens NA = 0.8
[49]	Hippocampal pyramidal neurons in culture (dissociated or slice not specified)	Two-photon	40 \times objective lens NA = 0.8, XY pixel size = $0.07 \times 0.07 \mu\text{m}$, 512×512 pixels in XY, 1.0 μm Z-spacing, 12 images per Z-stack
[51]	<i>In vivo</i> cranial window preparation, Thy-1 GFP M-line mouse	Two-photon	40 \times objective lens NA = 0.8, XY pixel size = $0.08 \times 0.08 \mu\text{m}$, 1024×1024 pixels in XY, 0.5 μm Z-spacing, 38–96 images per Z-stack
[52]	Lucifer yellow injected neurons in fixed brain slices of 200–400 μm	Confocal	100 \times objective lens NA = 1.4, XY pixel size = $0.05 \times 0.05 \mu\text{m}$, 512×512 pixels in XY, 0.11 μm Z-spacing, 100 optical sections
[55]	Not specified	Two-photon	XY pixel size = $0.05 \times 0.05 \mu\text{m}$, 512×512 pixels in XY, 0.1 μm Z-spacing, 18 optical sections
[56]	neurons in fixed brain slices of 200–400 μm after ballistic delivery of DiI	Confocal	100 \times objective lens NA = 1.4, XY pixel size = $0.06 \times 0.06 \mu\text{m}$, 512×512 pixels in XY, 0.12 μm Z-spacing, 120 optical sections
[57]	Brain slices labeled by ballistic delivery of DiI	Confocal	100 \times objective lens NA = 1.4, XY pixel size = $0.064 \times 0.064 \mu\text{m}$, 0.12 μm Z-spacing
[58]	Striatal neurons, labeling method not specified	Confocal	100 \times objective lens NA = 1.4, XY pixel size = $0.06 \times 0.06 \mu\text{m}$, 0.12 μm Z-spacing
[60]	Rat hippocampal neurons in culture expressing GFP or fixed brain section labeled by ballistic delivery of DiI	Confocal	100 \times objective lens NA = 1.2 for dissociated neurons, 63 \times objective lens NA = 1.4 for brain sections, XY pixel size = $0.07 \times 0.07 \mu\text{m}$, 0.2 μm Z-spacing
[61]	Live samples, without other information	Two-photon	60 \times objective lens NA = 0.9
[62]	Rat or mouse hippocampal neurons expressing Lifeact-Ruby in dissociated culture	Wide-field epifluorescence or confocal	60 \times objective lens NA = 1.4, 0.15 μm Z-spacing
[63]	Lucifer yellow injected neurons in human brain tissue	Confocal	63 \times objective lens
[64]	Medium spiny neurons in striatum, without other information	Confocal	XY pixel size = $0.064 \times 0.064 \mu\text{m}$, 512×512 pixels in XY, 0.12 μm Z-spacing
[65]	Neurons labeled by biolistic gene transfer of Dendra-2 in hippocampal organotypic slice cultures	Two-photon	60 \times objective lens NA = 0.9, XY pixel size = $0.019 \times 0.019 \mu\text{m}$, 1024×1024 pixels in XY, 0.3 μm Z-spacing
[66]	Not specified	Two-photon	XY pixel size = 0.019×0.019 or $0.024 \times 0.024 \mu\text{m}$, 0.3 μm Z-spacing
[68]	Layer III pyramidal neurons injected with lucifer yellow in fixed human brain sections	Confocal	63 \times objective lens, XY pixel size = $0.075 \times 0.075 \mu\text{m}$, 0.28 μm Z-spacing
[70]	Mouse hippocampal neurons in culture expressing GFP or labeled by DiI	SIM	100 \times objective lens NA = 1.49, XY pixel size = $0.032 \times 0.032 \mu\text{m}$, 512×512 pixels in XY, 0.12 μm Z-spacing, 63 optical sections after image reconstruction

Table 2. List of spine analysis procedures and performance

Ref. number	2D or 3D analysis	Method of spine detection	Method of spine segmentation	Spine shape measurement	Comparison with EM data	Comparison with other methods	Software/code availability
[33]	2D	Skeleton image analysis	NA	NA	NA	NA	NA
[34]	2D	Skeleton image analysis	NA	NA	NA	NA	NA
[35]	2D	Skeleton image analysis	Setting several rules to define spine base	Spine length measurement from skeleton image	NA	NA	NA
[36]	2D	Skeleton image analysis	Setting several rules to define spine base	Automated spine length measurement based on skeleton image	NA	This approach is implemented in NeuronIQ software. Comparison was made with Ref. [46] (less false negative, less false positive with 229 manually identified spines). Comparison was made with Ref. [36]	NA
[37]	2D	Skeleton image analysis	Borders defined by local intensity profile of spines	Spine length measured from skeleton image, spine volume estimated from approximation of segmented spine area to the sphere	Comparison with serial section EM reconstruction data based on different sample preparations	NA	NA
[38]	2D	Skeleton image analysis	Borders defined by local intensity profile of spines	NA	NA	Comparison was made with Ref. [34] (NeuronIQ software). NeuronIQ detects more spines but tends to detect non-spine structure and with inappropriate segmentation	NA
[39]	2D	Skeleton image analysis	Borders defined by local intensity profile of spines	Spine volume measurement performed, detailed method not provided	NA	NA	https://github.com/spinestool/Tracking-assisted_Spine_Detection
[40]	2D	Shaft boundary detection	Shaft boundary can be used as segmentation line	Spine length measured as distance from dendrite boundary to the spine's farthest pixel	NA	NA	NA
[43]	2D	Shaft boundary detection	Shaft boundary can be used as segmentation line	Spine classification by two-layered neural networks, the first extraction of shape features, the second network for classification, with three output nodes of mushroom, stubby, thin	NA	NA	NA

(Continued)

Table 2. Continued

Ref. number	2D or 3D analysis	Method of spine detection	Method of spine segmentation	Spine shape measurement	Comparison with EM data	Comparison with other methods	Software/code availability
[43]	2D/3D	Curvilinear structure detection	Setting several rules to define spine base	Spine length determined from backbone of spines, spine area determined from locally fitted binary image	NA	NA	NA
[46]	2D	Curvilinear structure detection	Borders defined by local intensity profile of spines	Spine length measured from spine centerline	NA	NA	NA
[47]	2D	Curvilinear structure detection	Setting several rules to define spine base	Spine shape expressed as integration of Zernike moments and 36 Zernike moments were used as spine features spine centerline is detected and spine length is measured	NA	NA	NA
[48]	3D	Skeleton image analysis	Borders defined by grouping voxels within spheres with a center at the spine tip	Spine length determined by the distance from the centroid of spine-shaft boundary to the farthest spine voxel, spine volume calculated as ratio of maximum spine intensity to maximum dendrite intensity multiplied by the focal volume	NA	Comparison was made with Ref. [34]	NA
[49]	3D	Skeleton image analysis	From the branch chains, those derived from spines were identified by the average length and radius of the structure surrounding the backbone	Five parameters (length, volume, basal radius, maximum radius, minimum radius) measured	NA	NA	NA
[51]	3D	Shaft centerline detection	Borders defined by grouping voxels within spheres with a center at the spine tip	NA	NA	NA	https://github.com/pankajmath/SpineDetectionAndExtraction
[52]	3D	Rayburst sampling	Borders defined by iterative addition of voxels from the spine tip, which was terminated by a predefined rule	Three parameters (aspect ratio, head-to-neck ratio, head diameter) measured and spines classified using the decision tree into mushroom, stubby and thin	NA	Comparison was made with Ref. [55]	https://biii.eu/neuronstudio
[53]	3D	Rayburst sampling	As in Ref. [50]	NA	NA	NA	NA
[54]	3D	Rayburst sampling	As in Ref. [50]	NA	NA	NA	NA
[55]	3D	Rayburst sampling	Borders defined by comparing the profiles of multiple spine cross-sections	Seven morphological parameters (head-to-neck ratio, head-to-length ratio, head diameter, neck diameter, maximum distance to dendrite surface, angle to xy-plane, length) measured, semi-supervised learning with training dataset applied for classification into mushroom, stubby and thin	NA	NA	NA

(Continued)

Table 2. Continued

Ref. number	2D or 3D analysis	Method of spine detection	Method of spine segmentation	Spine shape measurement	Comparison with EM data	Comparison with other methods	Software/code availability
[56]	3D	Gradient vector flow	Borders defined by fast marching algorithm	NA	NA	NA	NA
[57]	3D	3D surface feature	Spine-shaft borders defined by spine surface property	NA	NA	Comparison was made with Ref. [30], detection accuracy of this method was higher than the method of Ref. [50]	NA
[58]	3D	3D surface feature	Spine-shaft borders defined by spine surface property	NA	NA	Comparison was made with Ref. [43,50,54], improvement in sensitivity and specificity values by 3% compared with other three methods	NA
[60]	3D	3D gradual erosion	Borders defined by multi-scale opening algorithm	Four parameters (spine length, neck length, base-to-head distance, locally deepest point) measured, spine classification into mushroom, stubby, thin and spine-head protrusions by using a decision tree	NA	NA	NA
[61]	3D	Statistical modeling	NA	NA	Comparison with EM reconstructed data from identical dendrites was performed. Precision, 0.78; recall, 0.81 by this method, which are higher than the values (precision, 0.63; recall, 0.55) by the method of Ref. [34] (NeuronIQ software)	NA	NA
[62]	3D	3D tracing program in Imaris (Bitplane)	NA	Spine length, head width, neck width measured by Imaris software	NA	NA	NA
[63]	3D	3D tracing program in Imaris (Bitplane)	NA	Spine volume, area, length measured by Imaris software	NA	NA	http://gmrv.es/pyramidal-explore/
[65]	2D	NA	Spine shape expressed as a union of convex polytopes with their numbers and the number of half-spaces, the resulting shape representation was used for segmentation	Spine classification into three categories (mushroom, thin, stubby) based on 2D decision regions	NA	NA	https://github.com/mughanibin/Non-Parametric_Kernel_Density_Estimation
[66]	2D	NA	As in Ref. [63]	12 morphological features were used to perform cluster analysis, which produced four clusters containing at least one cluster not related to a known spine class	NA	NA	NA
[68]	3D	Manual detection	Manual segmentation	54 shape features extracted from the surface mesh data of spines, model-based clustering applied to a dataset of 7916 individual spines	NA	NA	NA
[70]	3D	3D fitting of dendritic shaft with elliptic cylinders, detection of spines as objects outside of the cylinders	Automatic segmentation after removal of the voxels belonging to dendritic shafts	3D surface meshes of spines created, ten geometrical parameters calculated and analyzed by principal component analysis, mushroom spines classified by support vector machine	Final spine surface mesh data compared with EM reconstruction data, showing high correlation in spine length, surface, volume	NA	https://www.nature.com/articles/s41467-019-09337-0

be predictable, as structural features of the spines themselves can also affect the performance.

Dendritic spine measurement by super-resolution imaging

Super-resolution imaging technology, which is advancing rapidly, could enable dendritic spine imaging with unprecedented accuracy and precision. Localization microscopy techniques such as PALM and STORM yield the highest resolution by estimating the positions of single molecules and are therefore suitable for describing the shapes of molecular assemblies such as PSDs and presynaptic active zones [71–73]. Localization microscopy requires a large number of molecular positions to achieve sufficient spatial resolution for detailed shape analysis of large structures. This problem can be overcome by using single-particle tracking photoactivation localization microscopy (sptPALM) [74] or universal point accumulation in nanoscale topography (*u*PAINT) [75], in which trajectories of large numbers of molecules are tracked on the surface of a live cell by continuous imaging. These techniques are useful for precisely identifying the boundaries of spine plasma membranes in 2D images of cultured neuronal samples, and their output can be easily combined with information about molecular localization of glutamate receptors and PSD scaffolding proteins [19,76].

STED microscopy can achieve a resolution of several tens of nanometers, and its spatial resolution in the z-direction can be improved by shaping STED light more isotropically around the focal point of the excitation beam [77,78]. Therefore, STED microscopy is the most promising approach for achieving *in vivo* super-resolution microscopy of dendritic spines [25,79]. When 2D STED microscopy was applied to spine shape changes after induction of structural plasticity, the results revealed a selective increase in the spine neck width, which may be involved in regulating the electrophysiological characteristics of spine synapses [7]. When combined with appropriate fluorescent probes for postsynaptic proteins, this approach can also be used to obtain detailed molecular distributions of synaptic proteins *in vivo* [30,80]. A new ImageJ plugin for STED microscopy-based spine analysis has been recently reported and may facilitate automated and unbiased analysis of spine structural changes related to synaptic plasticity [81].

3D-SIM microscopy offers a 2-fold increase in optical resolution in both the xy- and z-directions in comparison with conventional wide-field microscopy [82]. The improvement in resolution is moderate in comparison with localization and STED microscopy but may be sufficient to detect biologically important nanoscale features of dendritic spines. Recently, Kashiwagi *et al.* [70] reported a new analytical pipeline for quantitative analysis of spine morphology based on 3D-SIM imaging. Specifically, they performed 3D-SIM imaging of dendritic spines in cultured hippocampal neurons and then segmented dendrites and spines with multi-level thresholding based on Otsu's method [82] and geodesic active contours [82]. Direct comparison of reconstructed dendritic spines based on SIM images with those based on serial section EM images revealed that nanoscale surface features of dendritic spines were preserved in SIM-based reconstructions. The binary image stack of SIM was processed for automated spine detection by fitting the dendritic shaft with elliptic cylinders. By subtracting the volumes of dendritic shafts from the original dendritic volume, voxel clusters corresponding to spines were detected (Fig. 5). These voxels were further processed using the marching cube algorithm for isosurface triangulation [83].

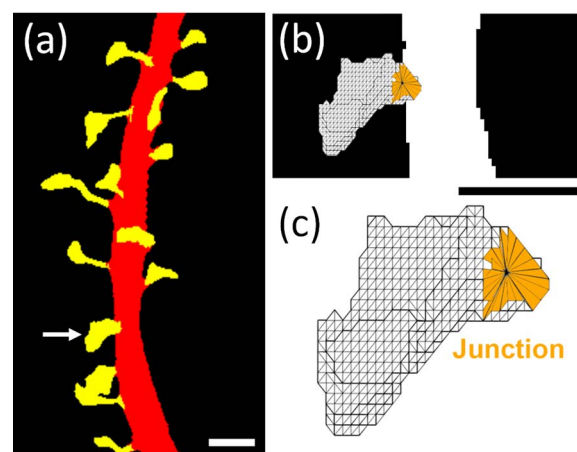


Fig. 5. SIM-based detection and segmentation of dendritic spines. (a) Reconstructed image of a dendrite based on 3D-SIM microscopy. Spines (yellow) and a shaft (red) were detected and segmented automatically. Bar, 1 μ m. (b) Generation of surface mesh data of a segmented dendritic spine (arrow in a). The spine–shaft junction is indicated by the yellow area. Bar, 1 μ m. (c) Enlarged image of the surface mesh.

The resultant 3D triangular mesh surfaces were used to extract 10 different geometrical parameters. Population data of these geometrical parameters from more than 1 thousand spines were then analyzed by PCA, followed by objective classification of mushroom spines by SVM. The accuracy of SVM-based classification was 85–90%, comparable to the performance of manual classification by human operators.

The spine geometry analysis proposed by Kashiwagi *et al.* [70] is useful for extracting the essential dynamic features of dendritic spines. Mapping the trajectories of individual spines in time-lapse imaging onto the feature space following PCA revealed that the spine population could be categorized into three groups with different morphological dynamics (Fig. 6a). Group 1 corresponds to small mushroom spines, which are stable in their morphology (Fig. 6b). Group 2 spines are large and stable mushroom spines with large fluctuations in volume. Finally, Group 3 consists of non-mushroom spines that tend to shrink and disappear. These three groups of spines also exhibited differential morphological characteristics. In particular, Group 2 spines had large concave surfaces on their heads, whereas this feature was rarely detected in Group 3 spines (Fig. 6c). The positions of these concave surfaces matched the positions of synaptic junctions, implying that the formation of stable junctions between pre- and postsynaptic compartments plays an important role in maintaining spines as well as in the transitions between different categories of spines. Results obtained with the analytical pipeline developed by Kashiwagi *et al.* demonstrate that detailed analysis of spine surface geometry by SIM-based imaging is a promising approach for revealing important structural parameters related to dendritic spine turnover, structural plasticity and synaptic efficacy.

Future directions

Over the past decade, researchers made a collective effort to establish widely applicable methods for objective and efficient measurement of the morphological features of dendritic spines. Consequently, we now have a variety of principles and methods for efficiently detecting, segmenting and quantitating dendritic spines in either 2D

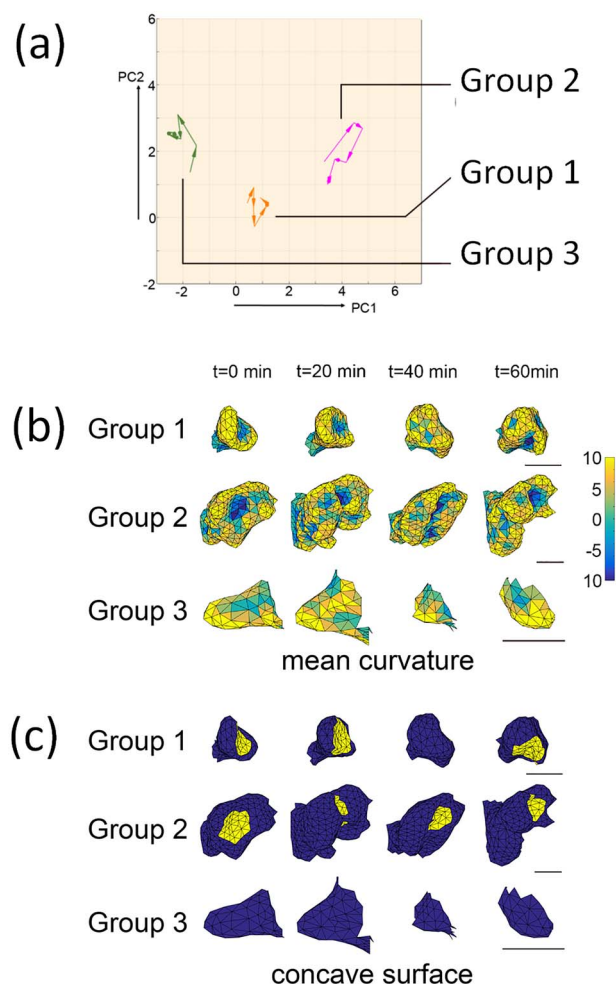


Fig. 6. SIM-based time-lapse imaging of spine nanostructure. (a) Temporal trajectories of three spine types (Groups 1, 2 and 3) that exhibited distinct dynamic shape changes during a 60 min time-lapse SIM imaging experiment. PC1 and PC2 are the first and second axes of PCA. (b). Surface mesh images of three spines that exhibited distinct dynamic shape changes during a 60 min time-lapse SIM imaging experiment. Surface color indicates mean curvature. (c) Mapping of the concave surface to spine heads for the three spine groups. Group 2 spines maintain a stable concave surface, whereas Group 3 spines tend to lack well-defined concave surfaces. Bars in (b) and (c), 500 nm.

or 3D imaging formats. Although individual protocols must be fine-tuned according to experimental goals and conditions, these methods greatly aid researchers in quantitating the morphology of a large number of spines. However, these methods are not yet perfect, and several persistent problems prevent direct comparison of the data among scientists working with different samples, imaging protocols and equipment. In this section, we describe these major problems and propose possible solutions.

In vivo spine measurement

Rapid progress in super-resolution microscopy has further increased the spatial resolution of light microscopy. Given the recent interest among neuroscientists in measuring dendritic spine morphology in the native tissue environment, super-resolution imaging based on laser scanning systems, such as 3D-STED microscopy, should be the imaging modality of choice for precise measurement of spine

morphology [77,78]. *In vivo* measurement of dendritic spine structure by 2D-STED microscopy has already been achieved [23,30,79,80], and extension of the method to 3D-STED microscopy may be possible in the near future. 3D-STED imaging requires a sufficient number of photons to be generated from the excitation volume, which is highly spatially restricted by the STED beam; consequently, it is critical to use bright fluorescent probes and a highly sensitive photon detection system. Recently, several approaches that reduce the excess activation of chromophores associated with super-resolution microscopy have been proposed. Reversible saturable optical fluorescence transition (RESOLFT) microscopy is a method using the photoswitching of fluorescent proteins to confine the volume of chromophore excitation. The lower dose of the light necessary for photoswitching in RESOLFT is advantageous in comparison with the relatively high dose necessary for de-excitation in STED [84,85]. It is also possible to utilize the two different off states of chromophores and reduce phototoxicity by selective induction into the second off state that is inert to the excess light in STED imaging [86]. Another challenge of *in vivo* 3D-STED imaging is suppression of tissue movement during laser scanning. One possible solution is laser scanning of a limited volume including only a small number of spines.

Conventionally, morphological analysis of spines is performed on 3D reconstructions of EM images. Over the past years, the efficiency and speed of EM reconstruction have improved significantly through the development of new scanning EM technologies such as FIB-SEM and SB-SEM [87,88]. In addition, array tomography, a technique for light microscopic observation of samples after thin sectioning of resin-embedded samples, has been developed [89]. Thin sectioning enables the application of localization microscopy to tissue samples: for example, the combination of thin sectioning of resin-embedded brain tissues with STORM imaging enabled researchers to identify synapse nanostructure in tissue sections [90]. The recently developed technique of expansion microscopy [91] raises the possibility of super-resolution imaging of synapses and spines in large volumes of brain samples [92]. Together, these developments in methods for sample preparation, tissue expansion and clearing, in combination with new imaging modalities, should allow researchers to obtain nanoscale structural data of thousands of synapses in large volumes of fixed tissue.

Identification of spine subclasses

Dendritic spines are highly diverse, with sizes ranging over more than an order of magnitude [92]. Spine structures vary from thin elongated filopodia-like protrusions to round mushroom-like shapes, and super-resolution imaging continues to reveal additional variability. As discussed above, the most commonly used classification system has three major categories: thin, mushroom and stubby; an additional category, filopodia, comprises non-spine dendritic protrusions. This subcategorization is useful because previous time-lapse imaging studies supported the idea that these three types reflect different dynamic states: mushroom spines are more mature and stable, whereas thin spines are immature and unstable [17,93]. On the other hand, some researchers have argued that spines exist on a morphological continuum and that simple categorization into three subtypes may be misleading [7,17]. The recent study by Kashiwagi *et al.* [70] identified continuous morphological variables in spine shape but also showed that spines with structural characteristics of mushroom spines form stable contact with presynaptic components but undergo dramatic volume fluctuations, suggesting a

correlation between the shape and functional properties of this spine population.

An independent approach to spine subtype classification is identification of spine population clusters after multi-dimensional analysis of structural parameters according to objective criteria, without manual evaluation. Luengo-Sanchez *et al.* [68] proposed model-based clustering of thousands of spines following creation of surface mesh data. Their results identified six separate groups, although the functional significance of these populations remains to be experimentally elucidated. Another study tried to correlate objectively defined spine population clusters with their dynamic properties [94]. In that work, the researchers measured 11 geometrical parameters of spine images acquired by confocal microscopy and then applied PCA to reduce the shape characteristics into the new 2D feature space. After objective clustering of spine populations, the entire population was classified into 10 clusters. Using these spine clusters, a shape transition model was generated, and its relevance to actual spine shape transitions was evaluated. This illustrates the utility of objective spine classification for improving our understanding of spine shape transition in large time-lapse datasets. Automated acquisition of time-lapse spine images should accelerate further development of computational approaches.

Structure–function relationship

Precise measurement of nanoscale spine morphology, combined with manipulation of spine functional status, will provide new insights into the relationship between spine function and structure. For example, when 2D-STED imaging was applied to dendritic spines [95], combined with two-photon uncaging of glutamate, which induces LTP [7], the results revealed that induction of LTP was associated with an increase in spine neck width and a concomitant decrease in length. These structural changes may decrease excitatory postsynaptic potential (EPSP), but may not affect the compartmentalization of signaling molecules in spines. This experiment clearly indicates that transient changes in the shape parameters of the spine neck may impact LTP and influence long-term changes in synaptic efficacy. In this sense, spine shape parameters may control meta-plasticity in neural circuit function. SIM-based nanoscale analysis of spines after induction of structural LTP, using glutamate uncaging, revealed a transient increase in the concave surface area of spine heads [70]. This shape change may reflect an increase in the area of the synaptic junctional membrane, which may facilitate recruitment of cell adhesion molecules to sites of pre- and postsynaptic interaction. This change in the shape of the spine head was blocked by an exogenously applied reagent that blocks the neurexin–neuroligin interaction, providing further evidence for the involvement of synaptic adhesion in maintaining and expanding the concave surface of the spine head. These two examples of plasticity-related structural changes in spines illustrate the power of precise structural measurement in facilitating our understanding of structure–function relationships in dendritic spines.

Funding

This work was supported by Grants-in-Aid for Scientific Research (17H01387 and 18H04727 to S.O.), Core Research for Evolutional Science and Technology from the Japan Science and Technology Agency (JPMJCR14W2 to S.O.), the Japan Agency for Medical Research and Development (JP19gm1310003 and JP19gm5010003

to S.O.) and the UTokyo Center for Integrative Science of Human Behavior (CiSHuB).

References

1. Sala C, and Segal M (2014) Dendritic spines: the locus of structural and functional plasticity. *Physiol. Rev.* 94: 141–188. doi: [10.1152/physrev.00012.2013](https://doi.org/10.1152/physrev.00012.2013).
2. Reichardt L F, and Lee S H (2010) Cell adhesion molecules at synapses. *Encycl. Neurosci.* 617–624. doi: [10.1016/B978-008045046-9.00355-7](https://doi.org/10.1016/B978-008045046-9.00355-7).
3. Togashi H, Sakisaka T, and Takai Y (2009) Cell adhesion molecules in the central nervous system. *Cell Adhes. Migr.* 29–35. doi: [10.4161/cam.3.1.6773](https://doi.org/10.4161/cam.3.1.6773).
4. Sorra K E, and Harris K M (2000) Overview on the structure, composition, function, development, and plasticity of hippocampal dendritic spines. *Hippocampus* 10: 501–511. doi: [10.1002/1098-1063\(2000\)10:5<501::AID-HIPO1>3.0.CO;2-T](https://doi.org/10.1002/1098-1063(2000)10:5<501::AID-HIPO1>3.0.CO;2-T).
5. Peters A, and Kaiserman-Abramof I R (1970) The small pyramidal neuron of the rat cerebral cortex. The perikaryon, dendrites and spines. *Am. J. Anat.* 127: 321–355. doi: [10.1002/aja.1001270402](https://doi.org/10.1002/aja.1001270402).
6. Hering H, and Sheng M (2001) Dendritic spines: structure, dynamics and regulation. *Nat. Rev. Neurosci.* 2: 880–888. doi: [10.1038/35104061](https://doi.org/10.1038/35104061).
7. Tønnesen J, Katona G, Rózsa B, and Nägerl U V (2014) Spine neck plasticity regulates compartmentalization of synapses. *Nat. Neurosci.* 17: 678–685. doi: [10.1038/nn.3682](https://doi.org/10.1038/nn.3682).
8. Hotulainen P, and Hoogenraad C C (2010) Actin in dendritic spines: connecting dynamics to function. *J. Cell Biol.* 619–629. doi: [10.1083/jcb.201003008](https://doi.org/10.1083/jcb.201003008).
9. Kneussel M, and Hausrat T J (2016) Postsynaptic neurotransmitter receptor reserve pools for synaptic potentiation. *Trends Neurosci.* 170–182. doi: [10.1016/j.tins.2016.01.002](https://doi.org/10.1016/j.tins.2016.01.002).
10. Cooney J R, Hurlburt J L, Selig D K, Harris K M, and Fiala J C (2002) Endosomal compartments serve multiple hippocampal dendritic spines from a widespread rather than a local store of recycling membrane. *J. Neurosci.* 22: 2215–2224. doi: <https://doi.org/10.1523/JNEUROSCI.22-06-02215.2002>.
11. Spacek J, and Harris K M (1997) Three-dimensional organization of smooth endoplasmic reticulum in hippocampal CA1 dendrites and dendritic spines of the immature and mature rat. *J. Neurosci.* 17: 190–203. doi: [10.1016/j.ijhydene.2009.07.120](https://doi.org/10.1016/j.ijhydene.2009.07.120).
12. Okabe S (2007) Molecular anatomy of the postsynaptic density. *Mol. Cell. Neurosci.* 503–518. doi: [10.1016/j.mcn.2007.01.006](https://doi.org/10.1016/j.mcn.2007.01.006).
13. Petersen J D, Chen X, Vinade L, Dosemeci A, Lisman J E, and Reese T S (2003) Distribution of postsynaptic density (PSD)-95 and Ca²⁺/Calmodulin-dependent protein kinase II at the PSD. *J. Neurosci.* 23: 11270–11278. doi: [10.1523/jneurosci.23-35-11270.2003](https://doi.org/10.1523/jneurosci.23-35-11270.2003).
14. Arellano J I, Benavides-Piccione R, DeFelipe J, and Yuste R (2007) Ultrastructure of dendritic spines: correlation between synaptic and spine morphologies. *Front. Neurosci.* 1: 131–143. doi: [10.3389/neuro.01.1.1.010.2007](https://doi.org/10.3389/neuro.01.1.1.010.2007).
15. Okabe S (2017) Fluorescence imaging of synapse dynamics in normal circuit maturation and in developmental disorders. *Proc. Jpn. Acad. Ser. B Phys. Biol. Sci.* 93: 483–497. doi: [10.2183/pjab.93.029](https://doi.org/10.2183/pjab.93.029).
16. Matsuzaki M, Honkura N, Ellis-Davies G C R, and Kasai H (2004) Structural basis of long-term potentiation in single dendritic spines. *Nature* 429: 761–766. doi: [10.1038/nature02617](https://doi.org/10.1038/nature02617).
17. Loewenstein Y, Yanover U, and Rumpel S (2015) Predicting the dynamics of network connectivity in the neocortex. *J. Neurosci.* 35: 12535–12544. doi: [10.1523/JNEUROSCI.2917-14.2015](https://doi.org/10.1523/JNEUROSCI.2917-14.2015).
18. Loewenstein Y, Kuras A, and Rumpel S (2011) Multiplicative dynamics underlie the emergence of the log-normal distribution of spine sizes in the neocortex in vivo. *J. Neurosci.* 31: 9481–9488. doi: [10.1523/JNEUROSCI.6130-10.2011](https://doi.org/10.1523/JNEUROSCI.6130-10.2011).
19. Chazeau A, Mehidi A, Nair D, Gautier J J, Leduc C, Chamma I, Kage F, Kechkar A, Thoumine O, Rottner K, Choquet D, Gautreau A, Sibarita J B, and Giannone G (2014) Nanoscale segregation of actin nucleation and

- elongation factors determines dendritic spine protrusion. *EMBO J.* 33: 2745–2764. doi: [10.15252/embj.201488837](https://doi.org/10.15252/embj.201488837).
20. Attardo A, Fitzgerald J E, and Schnitzer M J (2015) Impermanence of dendritic spines in live adult CA1 hippocampus. *Nature* 523: 592–596. doi: [10.1038/nature14467](https://doi.org/10.1038/nature14467).
 21. Dunaevsky A, Blazeski R, Yuste R, and Mason C (2001) Spine motility with synaptic contact. *Nat. Neurosci.* 4: 685–686. doi: [10.1038/89460](https://doi.org/10.1038/89460).
 22. Chen H, Tang A-H, and Blanpied T A (2018) Subsynaptic spatial organization as a regulator of synaptic strength and plasticity. *Curr. Opin. Neurobiol.* 51: 147–153. doi: [10.1016/j.conb.2018.05.004](https://doi.org/10.1016/j.conb.2018.05.004).
 23. ter Veer M J T, Pfeiffer T, and Nägerl U V (2017) Two-photon STED microscopy for nanoscale imaging of neural morphology in vivo. *Methods Mol. Biol. (Clifton, NJ)* 1663: 45–64. doi: [10.1007/978-1-4939-7265-4_5](https://doi.org/10.1007/978-1-4939-7265-4_5).
 24. Chéreau R, Tønnesen J, and Nägerl U V (2015) STED microscopy for nanoscale imaging in living brain slices. *Methods* 88: 57–66. doi: [10.1016/j.ymeth.2015.06.006](https://doi.org/10.1016/j.ymeth.2015.06.006).
 25. Berning S, Willig K I, Steffens H, Dibaj P, and Hell S W (2012) Nanoscopy in a living mouse brain. *Science* 335: 551–551. doi: [10.1126/science.1215369](https://doi.org/10.1126/science.1215369).
 26. Kilian N, Goryaynov A, Lessard M D, Hooker G, Toomre D, Rothman J E, and Bewersdorf J (2018) Assessing photodamage in live-cell STED microscopy. *Nat. Methods (Nature Publishing Group)* 15: 755–756. doi: [10.1038/s41592-018-0145-5](https://doi.org/10.1038/s41592-018-0145-5).
 27. Okabe S, Miwa A, and Okado H (2001) Spine formation and correlated assembly of presynaptic and postsynaptic molecules. *J. Neurosci.* 21: 6105–6114. doi: [10.1523/JNEUROSCI.21-16-06105.2001](https://doi.org/10.1523/JNEUROSCI.21-16-06105.2001).
 28. Okabe S, Kim H D, Miwa A, Kuriu T, and Okado H (1999) Continual remodeling of postsynaptic density and its regulation by synaptic activity. *Nat. Neurosci.* 2: 804–811. doi: [10.1038/12175](https://doi.org/10.1038/12175).
 29. Isshiki M, Tanaka S, Kuriu T, Tabuchi K, Takumi T, and Okabe S (2014) Enhanced synapse remodelling as a common phenotype in mouse models of autism. *Nat. Commun.* 5: 4742. doi: [10.1038/ncomms5742](https://doi.org/10.1038/ncomms5742).
 30. Masch J-M, Steffens H, Fischer J, Engelhardt J, Hubrich J, Keller-Findeisen J, D'Este E, Urban N T, SGN G, Sahl S J, Kamin D, and Hell S W (2018) Robust nanoscopy of a synaptic protein in living mice by organic-fluorophore labeling. *Proc. Natl. Acad. Sci. USA* 115: E8047–E8056. doi: [10.1073/pnas.1807104115](https://doi.org/10.1073/pnas.1807104115).
 31. Gray N W, Weimer R M, Bureau I, and Svoboda K (2006) Rapid redistribution of synaptic PSD-95 in the neocortex in vivo. *PLoS Biol.* 4: 2065–2075. doi: [10.1371/journal.pbio.0040370](https://doi.org/10.1371/journal.pbio.0040370).
 32. Benavides-Piccione R, Feraud-Espinosa I, Robles V, Yuste R, and Defelipe J (2013) Age-based comparison of human dendritic spine structure using complete three-dimensional reconstructions. *Cereb. Cortex* 23: 1798–1810. doi: [10.1093/cercor/bhs154](https://doi.org/10.1093/cercor/bhs154).
 33. Weaver C M, Hof P R, Wearne S L, and Lindquist W B (2004) Automated algorithms for multiscale morphology of neuronal dendrites. *Neural Comput.* 16: 1353–1383. doi: [10.1162/089976604323057425](https://doi.org/10.1162/089976604323057425).
 34. Rusakov D A, and Stewart M G (1995) Quantification of dendritic spine populations using image analysis and a tilting disector. *J. Neurosci. Methods* 60: 11–21.
 35. Bai W, Zhou X, Ji L, Cheng J, and Wong S T C (2007) Automatic dendritic spine analysis in two-photon laser scanning microscopy images. *Cytom. Part A* 71: 818–826. doi: [10.1002/cyto.a.20431](https://doi.org/10.1002/cyto.a.20431).
 36. Cheng J, Zhou X, Miller E, Witt R M, Zhu J, Sabatini B L, and Wong S T C (2007) A novel computational approach for automatic dendrite spines detection in two-photon laser scan microscopy. *J. Neurosci. Methods* 165: 122–134. doi: [10.1016/j.jneumeth.2007.05.020](https://doi.org/10.1016/j.jneumeth.2007.05.020).
 37. Son J, Song S, Lee S, Chang S, and Kim M (2011) Morphological change tracking of dendritic spines based on structural features. *J. Microsc.* 241: 261–272. doi: [10.1111/j.1365-2818.2010.03427.x](https://doi.org/10.1111/j.1365-2818.2010.03427.x).
 38. Rada L, Erdil E, Ozgurargunsah A, Unay D, Cetin M (2014) Automatic dendritic spine detection using multiscale dot enhancement filters and SIFT features. *2014 IEEE International Conference on Image Processing, ICIP 2014*, pp. 26–30. doi: [10.1109/ICIP.2014.7025004](https://doi.org/10.1109/ICIP.2014.7025004).
 39. Rada L, Kilic B, Erdil E, Ramiro-Cortés Y, Israely I, Unay D, Cetin M, and Argunsah A Ö (2018) Tracking-assisted detection of dendritic spines in time-lapse microscopic images. *Neuroscience* 394: 189–205. doi: [10.1016/j.neuroscience.2018.10.022](https://doi.org/10.1016/j.neuroscience.2018.10.022).
 40. Li Q, Sone S, and Doi K (2003) Selective enhancement filters for nodules, vessels, and airway walls in two- and three-dimensional CT scans. *Med. Phys.* 30: 2040–2051. doi: [10.1118/1.1581411](https://doi.org/10.1118/1.1581411).
 41. Su R, Sun C, Zhang C, and Pham T D (2014) A novel method for dendritic spines detection based on directional morphological filter and shortest path. *Comput. Med. Imaging Graph.* 38: 793–802. doi: [10.1016/j.compmedimag.2014.07.006](https://doi.org/10.1016/j.compmedimag.2014.07.006).
 42. Soille P, and Talbot H (2001) Directional morphological filtering. *IEEE Trans. Pattern Anal. Mach. Intell.* 23: 1313–1329. doi: [10.1109/34.969120](https://doi.org/10.1109/34.969120).
 43. Wang S, Chen M, Li Y, Zhang Y, Han L, Wu J, and Du S (2015) Detection of dendritic spines using wavelet-based conditional symmetric analysis and regularized morphological shared-weight neural networks. *Comput. Math. Methods Med.* 2015: 454076–454076.
 44. Steger G (1998) An unbiased detector of curvilinear structures. *IEEE Trans. Pattern Anal. Mach. Intell.* 20: 113–125. doi: [10.1109/34.659930](https://doi.org/10.1109/34.659930).
 45. Fan J, Zhou X, Dy J G, Zhang Y, and Wong S T C (2009) An automated pipeline for dendrite spine detection and tracking of 3D optical microscopy neuron images of in vivo mouse models. *Neuroinformatics* 7: 113–130. doi: [10.1007/s12021-009-9047-0](https://doi.org/10.1007/s12021-009-9047-0).
 46. Choy SK, Chen K, Zhang Y, Baron M, Teylan MA, Kim Y, Tong CS, Song Z, Wong ST. (2010) Multi scale and slice-based approach for automatic spine detection. *2010 Annual International Conference of the IEEE Engineering in Medicine and Biology Society, EMBC'10*. pp. 4765–4768. doi: [10.1109/IEMBS.2010.5626640](https://doi.org/10.1109/IEMBS.2010.5626640).
 47. Zhang Y, Zhou X, Witt R M, Sabatini B L, Adjeroh D, and Wong S T C (2007) Dendritic spine detection using curvilinear structure detector and LDA classifier. *NeuroImage* 36: 346–360. doi: [10.1016/j.neuroimage.2007.02.044](https://doi.org/10.1016/j.neuroimage.2007.02.044).
 48. Koh I Y Y, Lindquist W B, Zito K, Nimchinsky E A, and Svoboda K (2002) An image analysis algorithm for dendritic spines. *Neural Comput.* 14: 1283–1310. doi: [10.1162/089976602753712945](https://doi.org/10.1162/089976602753712945).
 49. Janoos F, Mosaliganti K, Xu X, Machiraju R, Huang K, and Wong S T C (2009) Robust 3D reconstruction and identification of dendritic spines from optical microscopy imaging. *Med. Image Anal.* 13: 167–179. doi: [10.1016/j.media.2008.06.019](https://doi.org/10.1016/j.media.2008.06.019).
 50. Dey TK, Sun J (2006) Defining and computing curve-skeletons with medial geodesic function. *Proceedings of the Fourth Eurographics Symposium on Geometry Processing—SGP '06*. pp. 143–152. doi: [10.1097/01.ju.0000145900.22849.1d](https://doi.org/10.1097/01.ju.0000145900.22849.1d).
 51. Singh P K, Hernandez-Herrera P, Labate D, and Papadakis M (2017) Automated 3-D detection of dendritic spines from in vivo two-photon image stacks. *Neuroinformatics* 15: 303–319. doi: [10.1007/s12021-017-9332-2](https://doi.org/10.1007/s12021-017-9332-2).
 52. Rodriguez A, Ehlenberger D B, Dickstein D L, Hof P R, and Wearne S L (2008) Automated three-dimensional detection and shape classification of dendritic spines from fluorescence microscopy images. *PLoS One* 3: e1997. doi: [10.1371/journal.pone.0001997](https://doi.org/10.1371/journal.pone.0001997).
 53. Rodriguez A, Ehlenberger D B, Hof P R, and Wearne S L (2006) Rayburst sampling, an algorithm for automated three-dimensional shape analysis from laser scanning microscopy images. *Nat. Protoc.* 1: 2152–2161. doi: [10.1038/nprot.2006.313](https://doi.org/10.1038/nprot.2006.313).
 54. Dumitriu D, Rodriguez A, and Morrison J H (2011) High-throughput, detailed, cell-specific neuroanatomy of dendritic spines using microinjection and confocal microscopy. *Nat. Protoc.* 6: 1391–1411. doi: [10.1038/nprot.2011.389](https://doi.org/10.1038/nprot.2011.389).
 55. Shi P, Huang Y, and Hong J (2014) Automated three-dimensional reconstruction and morphological analysis of dendritic spines based on semi-supervised learning. *Biomed. Opt. Express* 5: 1541. doi: [10.1364/BOE.5.001541](https://doi.org/10.1364/BOE.5.001541).
 56. Zhang Y, Chen K, Baron M, Teylan M A, Kim Y, Song Z, Greengard P, and Wong S T (2010) A neurocomputational method for fully automated 3D dendritic spine detection and segmentation of medium-sized spiny neurons. *NeuroImage* 50: 1472–1484. doi: [10.1016/j.neuroimage.2010.01.048](https://doi.org/10.1016/j.neuroimage.2010.01.048).

57. Qing Li Q, and Zhigang Deng Z (2012) A surface-based 3-D dendritic spine detection approach from confocal microscopy images. *IEEE Trans. Image Process.* 21: 1223–1230. doi: [10.1109/TIP.2011.2166973](https://doi.org/10.1109/TIP.2011.2166973).
58. He T, Xue Z, Kim Y, and Wong ST (2012) Three-dimensional dendritic spine detection based on minimal cross-sectional curvature. *Proceedings – International Symposium on Biomedical Imaging* 1639–1642. doi: [10.1046/j.1365-2656.1999.00334.x](https://doi.org/10.1046/j.1365-2656.1999.00334.x).
59. Saha P K, Basu S, and Hoffman E A (2016) Multiscale opening of conjoined fuzzy objects: theory and applications. *IEEE Trans. Fuzzy Syst.* 24: 1121–1133. doi: [10.1109/TFUZZ.2015.2502278](https://doi.org/10.1109/TFUZZ.2015.2502278).
60. Basu S, Saha P K, Roszkowska M, Magnowska M, Baczynska E, Das N, Plewczynski D, and Włodarczyk J (2018) Quantitative 3-D morphometric analysis of individual dendritic spines. *Sci. Rep.* 8: 3545. doi: [10.1038/s41598-018-21753-8](https://doi.org/10.1038/s41598-018-21753-8).
61. Blumer C, Vivien C, Genoud C, Perez-Alvarez A, Wiegert J S, Vetter T, and Oertner T G (2015) Automated analysis of spine dynamics on live CA1 pyramidal cells. *Med. Image Anal.* 19: 87–97. doi: [10.1016/j.media.2014.09.004](https://doi.org/10.1016/j.media.2014.09.004).
62. Swanger S A, Yao X, Gross C, and Bassell G J (2011) Automated 4D analysis of dendritic spine morphology: applications to stimulus-induced spine remodeling and pharmacological rescue in a disease model. *Mol. Brain* 4. doi: [10.1186/1756-6606-4-38](https://doi.org/10.1186/1756-6606-4-38).
63. Toharia P, Robles O D, Fernaud-Espinosa I, Makarova J, Galindo S E, Rodriguez A, Pastor L, Herreras O, De Felipe J, and Benavides-Piccione R (2016) PyramidalExplorer: a new interactive tool to explore morpho-functional relations of human pyramidal neurons. *Front. Neuroanat.* 9. doi: [10.3389/fnana.2015.00159](https://doi.org/10.3389/fnana.2015.00159).
64. Shi P, Zhou X, Li Q, Baron M, Teylan MA, Kim Y, WONG STC. (2009) Online three-dimensional dendritic spines morphological classification based on semi-supervised learning. *Proceedings – 2009 IEEE International Symposium on Biomedical Imaging: From Nano to Macro, ISBI 2009*. Pp. 1019–1022. doi: [10.1109/ISBI.2009.5193228](https://doi.org/10.1109/ISBI.2009.5193228)
65. Ghani M U, Mesadi F, Kanik S D, Argunşah A Ö, Hobbiss A F, Israely I, Ünay D, Taşdizen T, and Çetin M (2016) Dendritic spine classification using shape and appearance features based on two-photon microscopy. *J. Neurosci. Methods* 279: 13–21. doi: [10.1016/j.jneumeth.2016.12.006](https://doi.org/10.1016/j.jneumeth.2016.12.006).
66. Ghani MU, Erdil E, Kanik SD, Argunşah AO, Hobbiss AF, Israely I, Ünay D, Tasdizen T, Cetin M. (2016) Dendritic spine shape analysis: a clustering perspective. *Lecture Notes in Computer Science (Including Subseries Lecture Notes in Artificial Intelligence and Lecture Notes in Bioinformatics)*. pp. 256–273. doi: [10.1007/978-3-319-46604-0_19](https://doi.org/10.1007/978-3-319-46604-0_19)
67. Zhou D Y, Bousquet O, Lal T N, Weston J, and Scholkopf B (2004) Learning with local and global consistency. *Adv. Neural Inf. Proces. Syst.* 16: 321–328.
68. Luengo-Sanchez S, Fernaud-Espinosa I, Bielza C, Benavides-Piccione R, Larrañaga P, and DeFelipe J (2018) 3D morphology-based clustering and simulation of human pyramidal cell dendritic spines. *PLoS Comput. Biol.* 14: e1006221. doi: [10.1371/journal.pcbi.1006221](https://doi.org/10.1371/journal.pcbi.1006221).
69. Ghani M U, Mesadi F, Kanik S D, Argunşah A Ö, Hobbiss A F, Israely I, Ünay D, Taşdizen T, and Çetin M (2017) Dendritic spine classification using shape and appearance features based on two-photon microscopy. *J. Neurosci. Methods* 279: 13–21. doi: [10.1016/j.jneumeth.2016.12.006](https://doi.org/10.1016/j.jneumeth.2016.12.006).
70. Kashiwagi Y, Higashi T, Obashi K, Sato Y, Komiyama N H, Grant S G N, and Okabe S (2019) Computational geometry analysis of dendritic spines by structured illumination microscopy. *Nat. Commun.* 10: 1285. doi: [10.1038/s41467-019-09337-0](https://doi.org/10.1038/s41467-019-09337-0).
71. MacGillavry H D, Song Y, Raghavachari S, and Blanpied T A (2013) Nanoscale scaffolding domains within the postsynaptic density concentrate synaptic AMPA receptors. *Neuron* 78: 615–622. doi: [10.1016/j.neuron.2013.03.009](https://doi.org/10.1016/j.neuron.2013.03.009).
72. Sakamoto H, Ariyoshi T, Kimpara N, Sugao K, Taiko I, Takikawa K, Asanuma D, Namiki S, and Hirose K (2018) Synaptic weight set by Munc13-1 supramolecular assemblies. *Nat. Neurosci.* 21: 41–49. doi: [10.1038/s41593-017-0041-9](https://doi.org/10.1038/s41593-017-0041-9).
73. Tang A-H, Chen H, Li T P, Metzbowser S R, MacGillavry H D, and Blanpied T A (2016) A trans-synaptic nanocolumn aligns neurotransmitter release to receptors. *Nature* 536: 210–214. doi: [10.1038/nature19058](https://doi.org/10.1038/nature19058).
74. Manley S, Gillette J M, Patterson G H, Shroff H, Hess H F, Betzig E, and Lippincott-Schwartz J (2008) High-density mapping of single-molecule trajectories with photoactivated localization microscopy. *Nat. Methods* 5: 155–157. doi: [10.1038/nmeth.1176](https://doi.org/10.1038/nmeth.1176).
75. Giannone G, Hosy E, Levet F, Constals A, Schulze K, Sobolevsky A I, Rosconi M P, Gouaux E, Tampé R, Choquet D, and Cognet L (2010) Dynamic superresolution imaging of endogenous proteins on living cells at ultra-high density. *Biophys. J.* 99: 1303–1310. doi: [10.1016/j.bpj.2010.06.005](https://doi.org/10.1016/j.bpj.2010.06.005).
76. Nair D, Hosy E, Petersen J D, Constals A, Giannone G, Choquet D, and Sibarita J B (2013) Super-resolution imaging reveals that AMPA receptors inside synapses are dynamically organized in nanodomains regulated by PSD95. *J. Neurosci.* 33: 13204–13224. doi: [10.1523/JNEUROSCI.2381-12.2013](https://doi.org/10.1523/JNEUROSCI.2381-12.2013).
77. Wildanger D, Medda R, Kastrup L, and Hell S W (2009) A compact STED microscope providing 3D nanoscale resolution. *J. Microsc.* 236: 35–43. doi: [10.1111/j.1365-2818.2009.03188.x](https://doi.org/10.1111/j.1365-2818.2009.03188.x).
78. Lenz M O, Sinclair H G, Savell A, Clegg J H, Brown A C N, Davis D M, Dunsby C, Neil M A, and French P M (2014) 3-D stimulated emission depletion microscopy with programmable aberration correction. *J. Biophotonics* 7: 29–36. doi: [10.1002/jbio.201300041](https://doi.org/10.1002/jbio.201300041).
79. Pfeiffer T, Poll S, Bancelin S, Angibaud J, Inavalli V K, Keppler K, Mittag M, Fuhrmann M, and Nägerl U V (2018) Chronic 2P-STED imaging reveals high turnover of dendritic spines in the hippocampus in vivo. *eLife* 7: e34700. doi: [10.7554/eLife.34700](https://doi.org/10.7554/eLife.34700).
80. Wegner W, Mott A C, Grant S G N, Steffens H, and Willig K I (2018) In vivo STED microscopy visualizes PSD95 sub-structures and morphological changes over several hours in the mouse visual cortex. *Sci. Rep.* 8: 219. doi: [10.1038/s41598-017-18640-z](https://doi.org/10.1038/s41598-017-18640-z).
81. Levet F, Tønnesen J, Nägerl UV, and Sibarita JB (2020) SpineJ: A software tool for quantitative analysis of nanoscale spine morphology. *bioRxiv.* 174: 49–55. doi: [10.1101/764548](https://doi.org/10.1101/764548).
82. Gustafsson M G L, Shao L, Carlton P M, Wang C J R, Golubovskaya I N, Cande W Z, Agard D A, and Sedat J W (2008) Three-dimensional resolution doubling in wide-field fluorescence microscopy by structured illumination. *Biophys. J.* 94: 4957–4970. doi: [10.1529/biophysj.107.120345](https://doi.org/10.1529/biophysj.107.120345).
83. Lorensen W E, and Cline H E (1987) Marching cubes: a high resolution 3D surface construction algorithm. *Comput. Graph.* 21: 163–169.
84. Testa I, Urban N T, Jakobs S, Eggeling C, Willig K I, and Hell S W (2012) Nanoscopy of living brain slices with low light levels. *Neuron* 75: 992–1000. doi: [10.1016/j.neuron.2012.07.028](https://doi.org/10.1016/j.neuron.2012.07.028).
85. Tiwari D K, Arai Y, Yamanaka M, Matsuda T, Agetsuma M, Nakano M, Fujita K, and Nagai T (2015) A fast- and positively photoswitchable fluorescent protein for ultralow-laser-power RESOLFT nanoscopy. *Nat. Methods (Nature Publishing Group)*. 12: 515–518. doi: [10.1038/nmeth.3362](https://doi.org/10.1038/nmeth.3362).
86. Danzl J G, Sidenstein S C, Gregor C, Urban N T, Ilgen P, Jakobs S, and Hell S W (2016) Coordinate-targeted fluorescence nanoscopy with multiple off states. *Nat. Photonics* 10: 122–128. doi: [10.1038/nphoton.2015.266](https://doi.org/10.1038/nphoton.2015.266).
87. Denk W, and Horstmann H (2004) Serial block-face scanning electron microscopy to reconstruct three-dimensional tissue nanostructure. *PLoS Biol.* 2: e329. doi: [10.1371/journal.pbio.0020329](https://doi.org/10.1371/journal.pbio.0020329).
88. Knott G, Marchman H, Wall D, and Lich B (2008) Serial section scanning electron microscopy of adult brain tissue using focused ion beam milling. *J. Neurosci.* 28: 2959–2964. doi: [10.1523/JNEUROSCI.3189-07.2008](https://doi.org/10.1523/JNEUROSCI.3189-07.2008).
89. Collman F, Buchanan J, Phend K D, Micheva K D, Weinberg R J, and Smith S J (2015) Mapping synapses by conjugate light-electron array tomography. *J. Neurosci.* 35: 5792–5807. doi: [10.1523/JNEUROSCI.4274-14.2015](https://doi.org/10.1523/JNEUROSCI.4274-14.2015).
90. Sigal Y M, Speer C M, Babcock H P, and Zhuang X (2015) Mapping synaptic input fields of neurons with super-resolution imaging. *Cell* 163: 493–505. doi: [10.1016/j.cell.2015.08.033](https://doi.org/10.1016/j.cell.2015.08.033).
91. Chen F, Tillberg P W, and Boyden E S (2015) Expansion microscopy. *Science* 347: 543–548. doi: [10.1126/science.1260088](https://doi.org/10.1126/science.1260088).
92. Gao R, Asano S M, Upadhyayula S, Pisarev I, Milkie D E, Liu T-L, Singh V, Graves A, Huynh G H, Zhao Y, Bogovic J, Colonell J, Ott C M, Zugates C, Tappan S, Rodriguez A, Mosaliganti K R, Sheu S H, Pasolli

- H A, Pang S, Xu C S, Megason S G, Hess H, Lippincott-Schwartz J, Hantman A, Rubin G M, Kirchhausen T, Saalfeld S, Aso Y, Boyden E S, and Betzig E (2019) Cortical column and whole-brain imaging with molecular contrast and nanoscale resolution. *Science* 363: eaau8302. doi: [10.1126/science.aau8302](https://doi.org/10.1126/science.aau8302).
93. Yasumatsu N, Matsuzaki M, Miyazaki T, Noguchi J, and Kasai H (2008) Principles of long-term dynamics of dendritic spines. *J. Neurosci.* 28: 13592–13608. doi: [10.1523/JNEUROSCI.0603-08.2008](https://doi.org/10.1523/JNEUROSCI.0603-08.2008).
94. Bokota G, Magnowska M, Kuśmierczyk T, Łukasik M, Roszkowska M, and Plewczynski D (2016) Computational approach to dendritic spine taxonomy and shape transition analysis. *Front. Comput. Neurosci.* 10. doi: [10.3389/fncom.2016.00140](https://doi.org/10.3389/fncom.2016.00140).
95. Nägerl UV, Willig KI, Hein B, Hell SW and Bonhoeffer T (2008) Live-cell imaging of dendritic spines by STED microscopy. *Proc. Natl. Acad. Sci. USA* 105: 18982–18987. doi: [10.1073/pnas.0810028105](https://doi.org/10.1073/pnas.0810028105).